Carbon Energy

WILEY

CARBON ENERGY

RESEARCH ARTICLE OPEN ACCESS

UV to IR Continuous Photocatalytic Gas-Phase CO_2 Hydrogenation Over Ni-Doped Molybdenum Oxysulfide: An Experimental and Mechanistic Study

Arturo Sanz-Marco[1,2] | Javier Navarro-Ruiz[3] | Jose L. Hueso[1,2,4,5] | Iann C. Gerber[3] | Victor Sebastian[1,2] | Susanne Mossin[6] | David Nielsen[6] | Francisco Balas[1,2] | Jesus Santamaria[1,2]

[1]Instituto de Nanociencia y Materiales de Aragón (INMA), Department of Chemical Engineering and Environmental Technologies, University of Zaragoza and Consejo Superior de Investigaciones Científicas (CSIC), Zaragoza, Spain | [2]Networking Research Center in Biomaterials, Bioengineering and Nanomedicine (CIBER-BBN), Madrid, Spain | [3]Laboratory of Physics and Chemistry of Nano-Objects (LPCNO), Institut National des Sciences Appliquées (INSA-CNRS-UPS), Université de Toulouse, Toulouse, CEDEX 4, France | [4]Escuela Politécnica Superior, Universidad de Zaragoza, Huesca, Spain | [5]Instituto de Investigación Sanitaria (IIS) de Aragón, Zaragoza, Spain | [6]Department of Chemistry, Centre for Catalysis and Sustainable Chemistry, Technical University of Denmark, Kgs. Lyngby, Denmark

Correspondence: Francisco Balas (fbalas@unizar.es) | Jesus Santamaria (Jesus.Santamaria@unizar.es)

Received: 22 July 2024 | **Revised:** 23 September 2024 | **Accepted:** 12 October 2024

Funding: Financial support from the Spanish Ministry of Science and Universities through CEX2023-001286-S, PID2020-114926RB-I00, and CTQ2016-77144-R and the MICINN Scholarship.

Keywords: CO_2 utilization | DFT calculations | DRIFTS | EPR | MoS_2

ABSTRACT

The reduction of CO_2 toward CO and CH_4 over Ni-loaded MoS_2-like layered nanomaterials is investigated. The mild hydrothermal synthesis induced the formation of a molybdenum oxysulfide (MoO_xS_y) phase, enriched with sulfur defects and multiple Mo oxidation states that favor the insertion of Ni^{2+} cations via photo-assisted precipitation. The photocatalytic tests under LED irradiation at different wavelengths from 365 to 940 nm at 250°C rendered 1% CO_2 conversion and continuous CO production up to 0.6 mmol/(g_{cat} h). The incorporation of Ni into the MoO_xS_y structure boosted the continuous production of CO up to 5.1 mmol/(g_{cat} h) with a CO_2 conversion of 3.5%. In situ spectroscopic techniques and DFT simulations showed the O-incorporated MoS_2 structure, in addition to Ni clusters as a supported metal catalyst. The mechanistic study of the CO_2 reduction reaction over the catalysts revealed that the reverse water–gas shift reaction is favored due to the preferential formation of carboxylic species.

1 | Introduction

One of the principal conclusions of the COP28 celebrated in Dubai was that the global efforts to accomplish the objectives established by the Paris Agreement have been too slow in all areas of climate action committing governments around the world to decrease atmospheric concentrations of greenhouse gases (GHGs) [1, 2]. At this time, the worldwide CO_2 utilization potential is about 3.7 GTm per year, only representing 10% of the global CO_2 emissions [2]. The carbon capture and utilization (CCU) approach could tackle GHG emissions in an active and sustainable way, where CO_2 is taken up from the atmosphere and recycled in the form of fuels or value-added chemicals [3]. Among CCU technologies, the use of solar energy is an attractive pathway that has been explored using diverse catalytic procedures and reaction configurations [4–6]. These so-called solar fuels contribute to the carbon economy [7, 8], by converting atmospheric CO_2, together with H_2 from renewable sources, into value-added chemicals in a sustainable manner [9–11]. For these applications, the most studied photocatalyst is

titanium dioxide (TiO_2), even though its photocatalytic response must be improved with diverse surface and structural modifications as its band gap (~3.2 eV) limits the use of bare TiO_2 to the ultraviolet (UV) region [12]. Other catalysts that have been previously reported for CO_2 photoreduction include metals, metal oxides [13–15], graphitic carbon nitride [16], graphene oxide [17], carbons [18], or metal-organic frameworks [19] but the yields achieved are still too low to make a meaningful impact on CO_2 utilization. Therefore, the interest in developing novel and more efficient photocatalysts cannot be overlooked. This is being addressed through a variety of strategies that include advanced nanoscale design of materials at the nanoscale to minimize rapid electron-hole recombination and achieve wider spectrum light utilization [20], band gap tuning, morphology control induction of surface vacancies modification, and utilization of cocatalysts and heterojunctions [21].

Ultrathin two-dimensional (2D) materials are particularly attractive in photocatalysis and their impact is rapidly rising [22–24]. These 2D materials offer high levels of structural anisotropy with a great amount of exposed surface to the reaction environment. Ultrathin 2D transition metal chalcogenides have been investigated on the basis of their unique electrical and optical properties, being proposed for a variety of applications [25]. Particularly, the use of molybdenum sulfide (MoS_2) in catalysis has experienced increasing interest [26–28]. One of the reasons is the capability of MoS_2 to support a vast concentration of surface active sites, such as edge sites and vacancies, suitable for reactant adsorption, charge separation and migration, and photoreduction processes [29, 30]. Even though the MoS_2 basal plane is nearly inert [31], the formation of defects and deposition of metal ions in the surface layers could enhance its potential catalytic activity. For instance, Liu et al. reported that the intercalation of Cu^+ ions into the MoS_2 basal plane led to the activation of the catalyst for a continuous photocatalytic H_2 evolution reaction [32]. Hu et al. [33] have shown that few-layered MoS_2 favored the photocatalytic reduction of CO_2 toward methanol, due to the increased electron density in the S vacancies and unsaturated Mo-edge sites near the Fermi level. The formation of surface defects in the basal plane of MoS_2 reduced the coordination number of the metal ions and affected the electronic structure of the catalyst, thereby enhancing the photocatalytic response [34].

Despite its attractive properties for the photocatalytic CO_2 reduction and H_2 evolution reactions, MoS_2 is prone to deactivation via a "hole oxidation" mechanism [35]. A successful strategy to stabilize metal sulfide photocatalysts could be the production of oxysulfides with low crystallinity [36]. This approach enables the coexistence of several oxidation states for Mo atoms, along with mixed oxygen–sulfur units, through hybridization of S 3p and O 2p orbitals, as well as S_2^{2-} ions [37]. Literature shows that metal oxide and sulfide nanostructures can act as catalysts for diverse processes. For instance, MoS_2 nanosheets evolve upon light irradiation into an oxygen-deficient MoS_2/MoO_{3-x} oxysulfide structure, whose versatility has been exploited in a dual capacity as photocatalyst in the CO_2 reduction to CO reaction and for surface enhanced Raman scattering detection thanks to the stabilization of surface plasmon and hot electron generation around the oxygen vacancies [38]. Also, transition metal oxysulfides have shown an enhanced capacity for photocatalytic water splitting and improved resistance toward corrosion under different reaction conditions [39].

Here, we report on the preparation of Ni-doped molybdenum oxysulfide nanolayers with low crystalline structure, obtained through mild hydrothermal techniques followed by photo-assisted Ni precipitation. These materials exhibited enhanced photocatalytic activity for continuous gas-phase CO_2 reduction under a wide range of illumination wavelengths beyond UV light. Furthermore, CO_2 conversion levels reached 3.5% with continuous production of CO and CH_4 in the millimolar range. Using in situ electron paramagnetic resonance (EPR) and diffuse reflectance Fourier-transformed infrared spectroscopic (DRIFTS) analysis, we discuss the electronic and chemical environments of the surface of MoO_xS_y nanolayers with mixed-valence Mo cations and S_2^{2-} anions, as well as surface S-vacancies and Ni nanoparticles. This complex electronic and chemical environment holds a strong influence on gas adsorption under reaction conditions. We also demonstrate that keeping the low crystallinity nature of the layered Mo oxysulfide is vital to obtaining a positive photocatalytic performance and paving the way for the preparation of low-crystallinity full-spectrum photocatalytic materials with an elevated number of surface defects to accommodate CO_2 and its subsequent conversion into benefit by-products. Finally, density functional theory (DFT) simulations established the most favored catalyst configuration to accommodate Ni species, established the most suitable H_2 dissociation scenarios, and established the preferential CO_2 reaction pathways toward preferential CO production.

2 | Results and Discussion

2.1 | Structural Analysis of Molybdenum Oxysulfides

After the hydrothermal synthesis, the material structure consisted of a limited long-range order of randomly stacked molybdenum oxysulfide layers. The X-ray diffraction (XRD) peaks around 13°, 38°, and 58° were assigned to (0002), (10$\bar{1}$ 3), and (10$\bar{1}$ 7) reflections of a 2H–MoS_2 phase, respectively, whereas the increase in the peak intensity around 32° was attributed to the (10$\bar{1}$ 3) planes of MoS_2 and (2$\bar{1}$ $\bar{1}$ 1) of hexagonal MoO_3 structure (Figure 1A). energy dispersive X-ray spectroscopy (EDS) mapping (Supporting Information S1: Figure S1) shows that the photodeposition led to low Ni loading, with a high dispersion of the metal over the surface of MoO_xS_y. Interestingly, the photodeposition of Ni cations increased the crystallinity of the materials, showing an enhancement in the intensity of the (0002) peak. This might suggest a slight rearrangement of the layered structure upon the introduction of the Ni clusters. XRD diffractograms after the reaction pointed to an enhancement of the crystallinity of both Ni-free and Ni-containing catalysts following the photocatalytic tests. The narrowing of XRD peaks and the shift toward higher diffraction angles implied the reorganization of layer stacking, which was mainly observed in the interlayer peak of the 2H–MoS_2 structure at 14° 2θ (Figure 1A). This effect became more evident in the Ni-doped catalyst, suggesting that Ni in the oxysulfide surface layers could induce recrystallization through the formation of a mixed Ni and Mo sulfide surface (Figure 1F). Raman spectra showed the E^1_{2g} and the A_{1g} vibrational modes characteristic of the 2H–MoS_2 phase at 380 and 410 cm^{-1}, respectively [40, 41]. Two

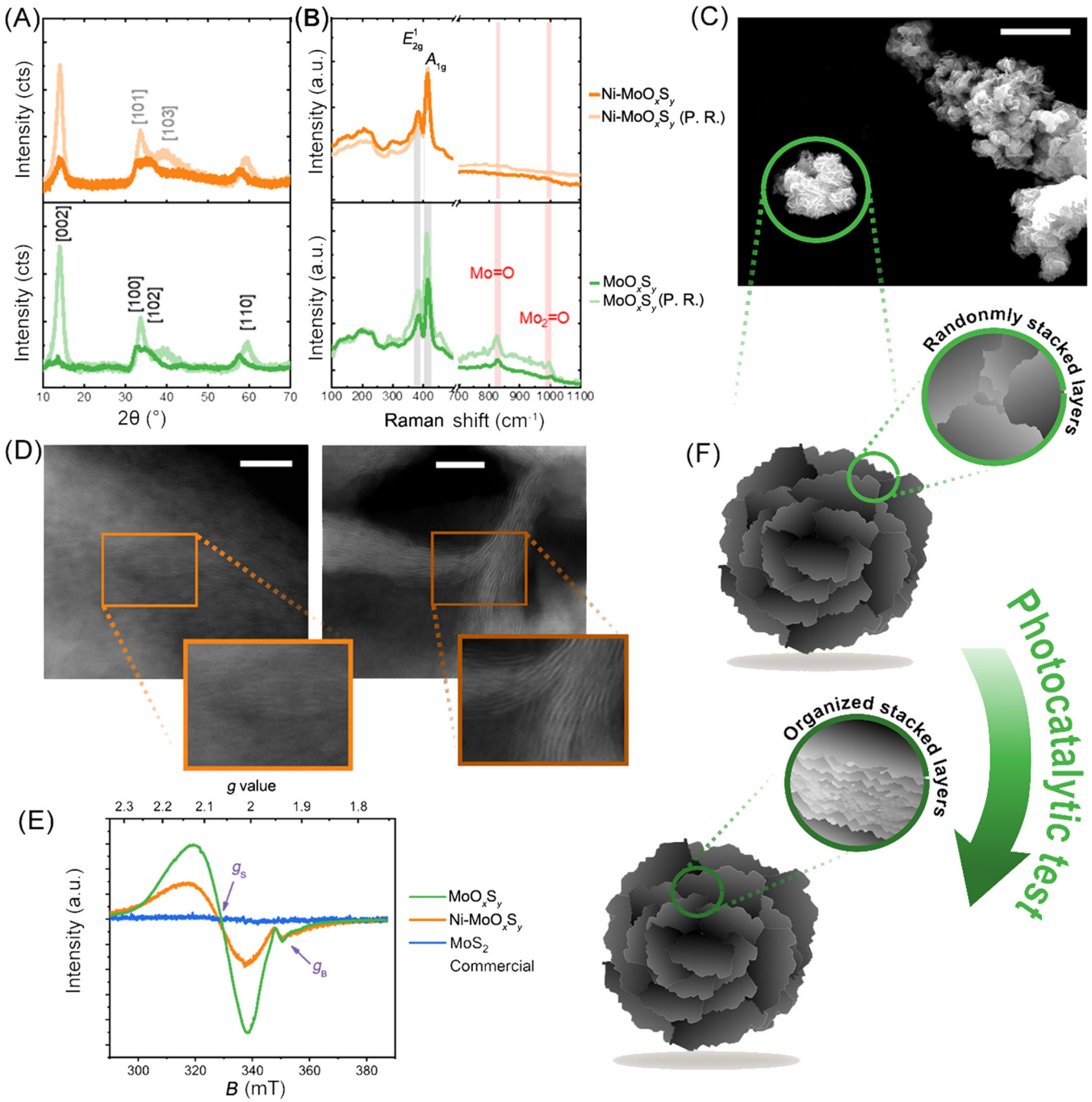

FIGURE 1 | (A) XRD patterns of as-synthesized Ni–MoO_xS_y (orange line) and MoO_xS_y (green line) catalysts, where the light-colored lines correspond to the patterns obtained after the photocatalytic CO_2 reduction over both materials (P. R. represents post-reaction), showing the increase in the intensity of (002), (101), and (103) reflections after reaction tests; (B) Raman spectra of as-synthesized Ni–MoO_xS_y (orange) and MoO_xS_y (green) catalysts showing the characteristic $E_{2g}{}^1$ and A_{1g} vibrational modes of 2H–MoS_2 layered structure as well as the modes of Mo═O and Mo_2–O groups. The light-colored lines correspond to the spectra obtained for catalysts after the photocatalytic CO_2 reduction over both materials, showing the increase in the intensity of oxidized species after reaction tests; (C) SEM image of Ni–MoO_xS_y showing the formation of 1 μm multilayered and polyorientated aggregates (scale represents 1 μm); (D) HAADF-STEM image of as-synthesized Ni–MoO_xS_y (orange) showing the low crystalline nature of the layered material, whose stacking ordering increases after the CO_2 reduction tests (brown) (scales represent 10 nm), where it regains the MoS_2-like layered structure; (E) EPR spectra of MoO_xS_y (green line), Ni–MoO_xS_y (orange line), and crystalline MoS_2 (blue line) indicating the signals attributed to the anisotropic (g_s) and symmetric (g_B) tensors of the Mo^{5+} cations, which are absent in diamagnetic Mo^{4+} of MoS_2; (F) schematic representation of the layer rearrangement of catalysts upon CO_2 hydrogenation tests at 250°C.

additional bands at 828 and 997 cm^{-1} were attributed to the vibration modes of MoO_3, namely, the double coordinated bridging oxygen and the terminal oxygen (see Figure 1B) [42]. These results suggest that the mild hydrothermal synthesis led to a mixed-valence molybdenum oxysulfide phase with a low-crystalline MoS_2-like structure. The SEM images (Figure 1C) showed that the fresh solids consisted of nanosized agglomerates with randomly stacked layers at the surface. This was further confirmed by high-angel annular dark-field scanning transmission electron microscopy (HAADF-STEM) analysis (Figure 1D), where the layers of the Ni-containing materials were difficult to identify due to low crystallinity. The HAADF-STEM image obtained after those tests confirm the rearrangement of the layered structure, increasing the stacking of the layers. In both cases, the distance between layers measured in the HAADF-STEM images is 7.57 ± 0.12 Å. This interlayer distance is in accordance with the distance derived from the (0002) XRD peak, which gives 6.33 ± 0.22 Å. Moreover, the increased intensity of the (10$\bar{1}$ 3) and (10$\bar{1}$ 7) reflections suggests a higher periodicity in the basal planes of the layers of the material (see also Figure 1D). The X-ray photoelectron spectroscopy (XPS) spectrum corresponding to the Mo 3d region revealed the coexistence of three oxidation states; moreover, EPR spectra confirmed the oxidation state of Mo in the solids. These showed two different signals (Figure 1E): the anisotropic tensor (g_S, with components $g_x = 2.02$, $g_y = 2.021$, and $g_z = 2.17$) and the axially symmetric tensor (g_B, with $g_\perp = 1.94$ and $g_{||} = 1.89$ components), respectively, assigned to local defects (V_S) in the sulfur sublattice [43] and to Mo^{5+} paramagnetic sites located in the nanocrystalline domains of sulfides [44]. For the sake of comparison, a crystalline sample of commercially available MoS_2 (Sigma Aldrich, St. Louis, Missouri) was measured under the same conditions, showing no EPR signals as was expected for the $4d^2$ electronic configuration of Mo^{4+} (Figure 1F) [45].

The oxidation state of Mo and S, together with that of Ni clusters, on the surface played a fundamental role in the catalytic performance of the materials. Changes in the oxidation state during reaction suggested the surface rearrangement upon CO_2 and H_2 adsorption and reaction. XPS spectra of pristine catalysts showed three doublet signals in the Mo 3d region, corresponding to the Mo^{4+} (229.25 and 232.2 eV), Mo^{5+} (230.3 and 232.9 eV), and Mo^{6+} (233.7 and 236.6 eV) (Figure 2). For each doublet, the area ratio between $3d_{5/2}$ and $3d_{3/2}$ was approximately 3/2 and the split-orbit separation was close to 3 eV, characteristic of the Mo 3d levels [46]. Those signals were assigned to MoS_2, MoO_xS_y, and MoO_3 phases, respectively [47, 48]. The signal attributed to the oxysulfide remained undetected in the spectra corresponding to materials after the catalytic tests (Figure 2D), and the Mo^{6+} ratio on the surface dropped from 32% to 20%. The S 2p signal revealed an interesting evolution of the oxidation state of sulfur on the surface (Figure 2B). Before the photocatalytic runs, the materials displayed

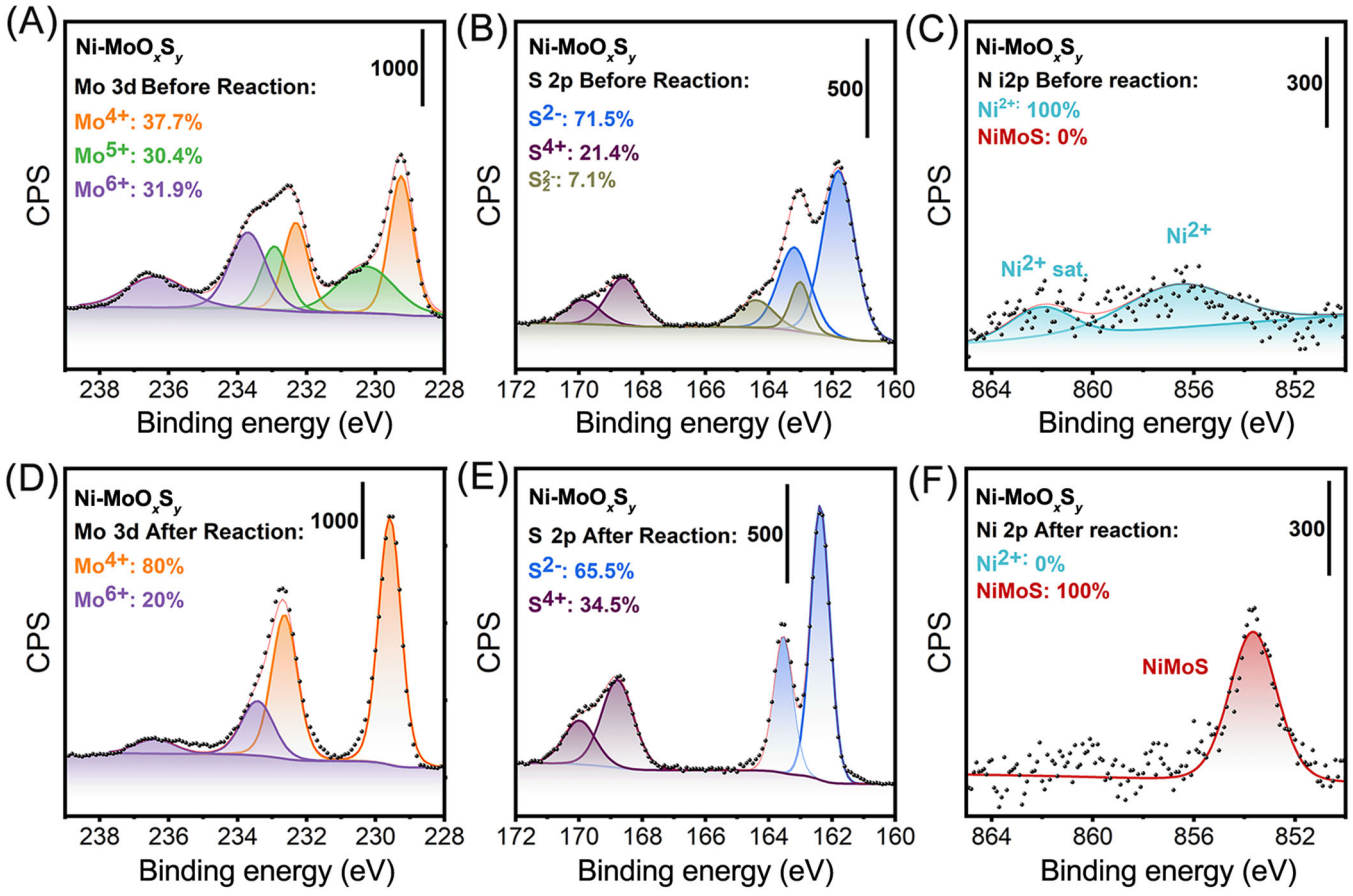

FIGURE 2 | X-ray photoemission spectra corresponding to (A) Mo 3d and (B) S 2p bands of as-synthesized MoO_xS_y, showing the presence of multiple oxidation states of Mo and S ions on the material surface. (C) The Ni 2p spectrum of Ni–MoO_xS_y shows that photodeposition leaves Ni^{2+} cations on the surface around surface vacancies. After photocatalytic CO_2 reduction tests ($CO_2/H_2 = 1/4$, 15 mL/min in standard temperature and pressure (STP), $p = 1.7$ bar), the Mo 3d (D) and S 2p (E) spectra show the disappearance of Mo^{5+} and S_2^{2-} species, as well as the rearrangement of Ni cations (F) into a surface NiMoS phase.

basal plane sulfide (S^{2-}) ligands in MoS_2-like layers (161.79 and 163.19 eV), together with the disulfide units (S_2^{2-}), attributed to MoO_xS_y (163.01 and 164 eV) and the S^{4+} corresponding to the sulfate group (168.59 and 169.87 eV) [46]. The increase of the sulfate contribution was probably a result of the exposure to water molecules generated during the CO_2 reduction, via reverse water-gas shift (RWGS) reaction ($CO_2 + H_2 \rightarrow CO + H_2O$, $\Delta_r H^0 = 41$ kJ/mol) and Sabatier's reaction ($CO_2 + 4H_2 \rightarrow CH_4 + 2H_2O$, $\Delta_r H^0 = -165.1$ kJ/mol), as well as to the exposure to air moisture before XPS analysis. However, CO_2 hydrogenation over MoO_xS_y led to the removal of S_2^{2-} signals in the XPS spectra and a slight blue shift of S^{2-} peaks. This suggested the crystal rearrangement in the substrates upon photocatalytic tests, altering the oxidation state of sulfur in the surface. In the spectra of Ni-doped samples, Mo 3d and S 2p regions showed a similar trend during the photocatalytic activity tests (data not shown). As for the Ni 2p region (Figure 2C), low signals could be discerned at 856.6 and 862 eV, corresponding to Ni^{2+} species and a satellite peak in the pristine materials [49]. After CO_2 reduction tests over these catalysts, the entire signal shifted to 853.6 eV (Figure 2F), attributed to the formation of a mixed NiMoS phase in the surface [50]. The low amount of Ni deposited over the surface of the MoO_xS_y and its high dispersion led to the low signal obtained in the XPS Ni 2p region. Even so, the total peak area detected under both conditions was similar, suggesting the incorporation of Ni cations. This crystalline reorganization and the disappearance of Mo^{5+} and S_2^{2-} signals pointed to the reorganization of MoS_2 and MoO_3 domains in the catalyst surface during the reaction, leaving a surface with a high density of sulfur vacancies. For Ni–MoO_xS_y, the crystal reorganization, together with the reductive atmosphere, led to the reordering of the Ni clusters on the surface at the expense of the Mo and S vacancies left by the MoS_2 domains upon reorganization.

2.1.1 | In Situ EPR Spectroscopy

EPR spectra recorded in He atmosphere (Supporting Information S1: Experiment I) showed values of the g_B signal corresponding to Mo^{5+} sites (Figure 3). This value significantly increased after heating up to 250°C (note that the EPR spectrum in Figure 3A was scaled down by a factor of 15). This suggested an increase in the crystallinity of the sample upon heating, increasing the density of Mo^{5+} domains. This effect was less evident for Ni–MoO_xS_y, yet the small g_e signal at 2.0034 pointed out that the Ni incorporation enhanced the free-electron density. The reductive atmosphere induced the appearance of a hyperfine signal and g_B signal decay (Figure 3C,D), in agreement with the absence of Mo^{5+} in XPS spectra after photocatalytic tests (see above and Figure 2D). In addition, the anisotropic signal (g_A) at $g_x = 1.987$, $g_y = 1.9807$, and $g_z = 1.877$, overlapping with the g_S signal at $g_x = 1.994$, $g_y = 2.0009$, and $g_z = 2.059$, pointed to the presence of Mo^{5+} cations at local defects in the molybdenum sublattice, such as cut-off or dangling bonds [44]. Both g_A and g_B observed after heating the sample under 80%-H_2 stream suggested the evolution of oxysulfide domains toward either MoS_2 or MoO_3 crystalline domains, similar to what was observed in the XPS spectra. This crystalline restructuring led to a higher density of S^{2-} defects in the layers of the MoS_2-like structure. For Ni–MoO_xS_y, however, experiments under H_2 led to the complete disappearance of EPR signals (Figure 3D) related to Mo. However, one can notice the

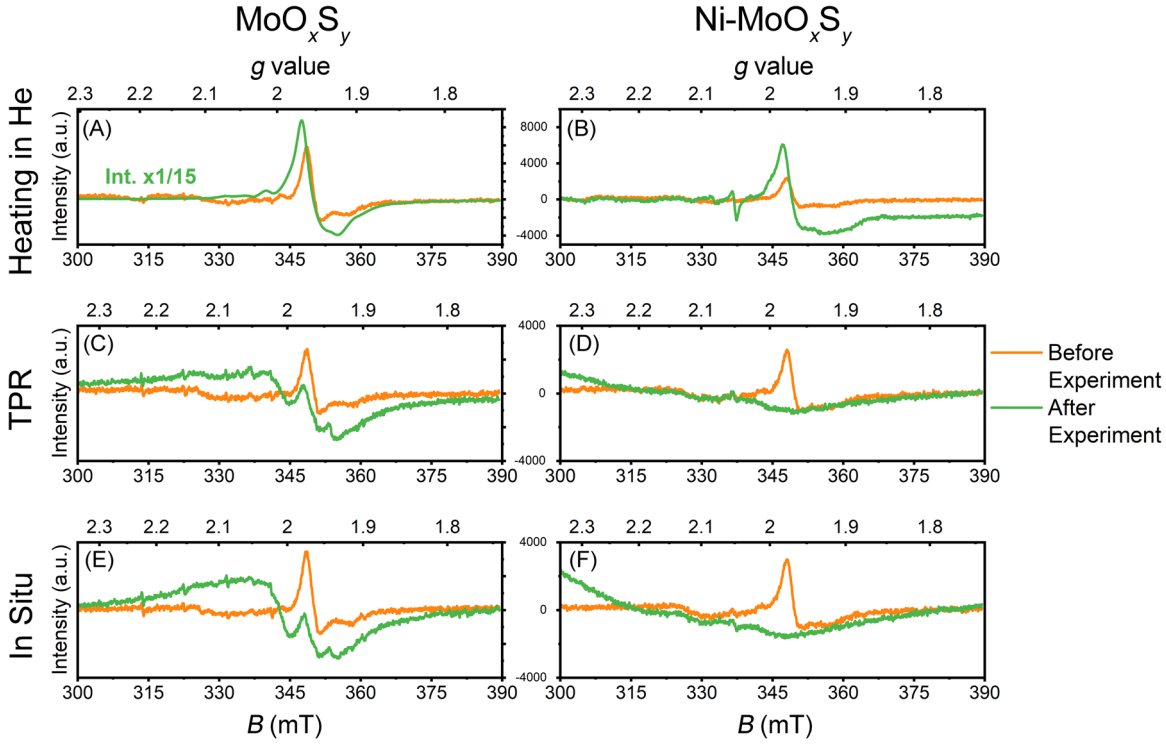

FIGURE 3 | EPR spectra of MoO_xS_y and Ni–MoO_xS_y obtained before (orange) and after (green) each in situ EPR experiment. (A, B) Heating in He at 250°C; (C, D) temperature programmed reduction in He/H_2 mixture (20/80 vol%) at 250°C, and (E, F) in situ CO_2 reduction experiment in a CO_2/H_2 mixture (20/80 vol%) at 250°C.

broad signal centered approximately at $g = 2.2$ corresponding to the unpaired electron in the $3d_{x^2-y^2}$ orbital of Ni^+ [51]. These results, in accordance with the XPS analysis, suggested that the Ni atoms were located around the vacancies in the sulfur sublattice, leading to a noticeable increase in the photocatalytic activity of Ni-doped materials.

2.2 | DFT Modeling of the Ni-Doped Molybdenum Oxysulfides

For a better understanding of the origin of the structure-dependent activity and selectivity of Ni–MoS_xO_y catalysts toward CO at the atomic level, a series of DFT simulations were carried out. While the catalytic performances of basal plane-based MoS_2 systems typically show higher selectivity for the hydrogenation of CO_2 to methanol [33], it has been reported that the edges act as catalytic active sites [52, 53]. This would suggest that the MoS_2 edge terminations were potentially active for the RWGS reaction, although their activity and stability would depend on the edge structure, temperature, and reaction conditions [54].

Aiming at edge chemistry, the 2H–MoS_2 structure could basically have two different terminations, the $(10\bar{1}\,0)$ Mo-edge and the $(\bar{1}\,010)$ S-edge planes (Figure 4). According to sulfur vacancies (V_S) identified in the in situ EPR spectra (Figure 3), together with XPS Ni 2p analysis (Figure 2), it can be assumed that Ni was in similar proportions as V_S sites. These results, combined with a Ni loading between 0.8% and 1.1%, suggested that the degree of sulfur coverage for edge structures is total, hereinafter referred to as Mo-100S or S-100S (Mo and S edges were 100% saturated with S dimers). On the other hand, the mild conditions used for materials preparation prevented the formation of a pure MoS_2 phase and allowed Mo–O bonds through oxygen incorporation, without altering the 2H–MoS_2 structure [55]. The substitution of oxygen for sulfur (equivalent to 11.2% for a final S:O ratio of 7.9% after XRD data) was carried out along the edge planes of the 2H–MoS_2 lattice. Up to 20 different models were generated and optimized for each of the terminations, selecting the atoms to be replaced based on a heterogeneous random distribution where the upper S layers were more oxidized than the inner regions. The heat map for relative stabilities of oxygen-incorporated Mo-100S and S-100S edges (see Supporting Information) showed that Mo-terminated models spanned a notably wider energy range than S-terminated ones. The stability of the former could depend to a greater extent on the position of the surface O* (surface-adsorbed O atom). To identify partially and completely oxidized domains similar to those detected experimentally, all models were sorted based on the average first nearest-neighbor (NN) O–O distance (see Supporting Information). Unlike Mo-100S structures, which asymptotically stabilized at long interatomic distances, the S-100S structures showed the opposite trend revealing that the as-synthesized oxysulfides exhibited sulfurized terminations (Figure 4 and Supporting Information S1: Figure S2D,E).

These surface defects influenced the physical and electronic properties of the materials, in addition to inducing specific sites for metal deposition. Since the concentration of V_S was low, the elimination of an S atom on the two terminations of the model oxygen-incorporated MoS_2 supports (equivalent to 1.1%) was subsequently analyzed. Formation energies and corresponding structures for V_S on the fully sulfur-covered edges (Supporting Information S1: Figure S3) suggested that for Mo-100S the only thermodynamically plausible scenarios were those caused by the loss of sulfur from the terminal Mo(SO) dimers with average formation energies of -19.5 kcal mol^{-1} (see S1 and S6 in Supporting Information S1: Figure S3A). The removal of sulfur from terminal Mo(S_2) dimers led to unfavorable processes (formation energies between 6 and 15 kcal mol^{-1}), which would

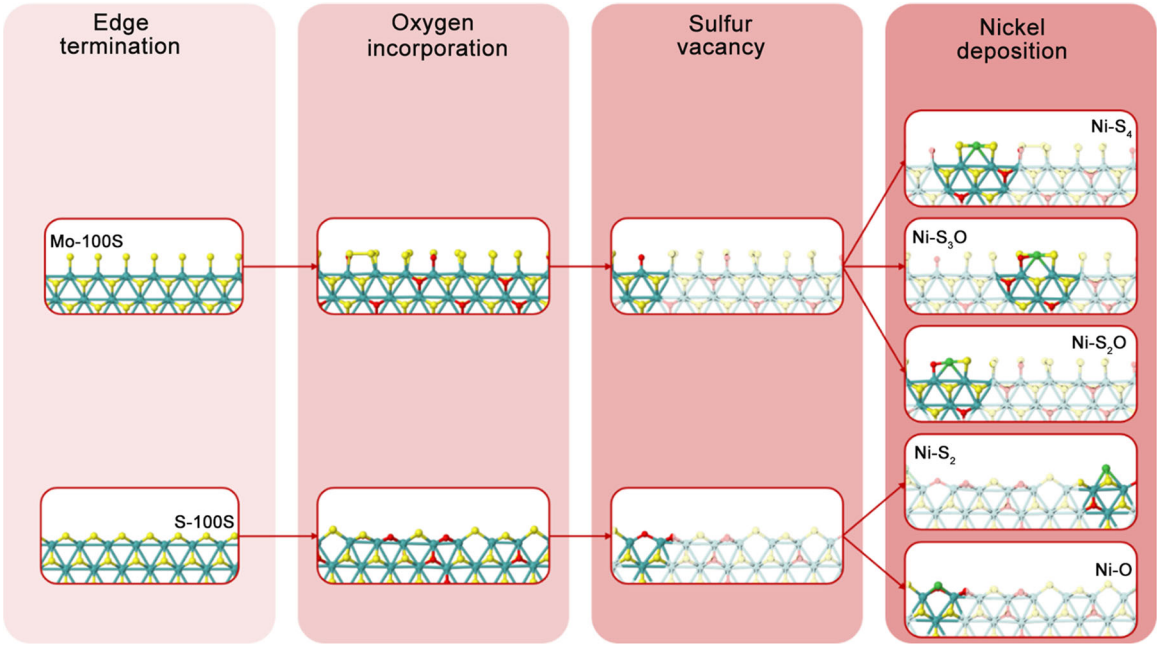

FIGURE 4 | Hierarchy chart for the design of Ni-supported molybdenum oxysulfide catalysts. Atomic color scheme: Mo (Verdigris); Ni (Apple); S (Daffodil); O (Candy Apple Red).

point to a lower density of Mo=S species and a high stability of the disulfide motifs [56]. For S-100S, however, all possible scenarios were hardly feasible, although Mo–O–Mo and Mo–SO–Mo species could appear under reaction conditions given their almost negligible energy costs (barely 0.9 kcal mol^{-1}, see S1 and S2(S3) in Supporting Information S1: Figure S3B).

As for nickel deposition on the sulfur-defective molybdenum oxysulfide systems, it could be assumed that Ni atoms were dispersed along the surface with no aggregates or large deposits (see HAADF-STEM images in Figure 1D). Therefore, the inclusion of a Ni single atom (Ni_{SA}) was assumed upon the deposition process for modeling purposes. Binding energies and corresponding structures for Ni_{SA} on edge S-vacancy models (Supporting Information S1: Figure S4) pointed to a unique nature of the terminal coordinative species, leading the Mo-100S edge to thermodynamically more favorable situations than the S-100S edge [57]. This structural stability could be attributed to the high coordination environment of Ni, providing the binding energies as Ni–$S_4^{Mo-100S}$ (square planar) > Ni $-S_3O^{Mo-100S}$ (square planar) > Ni–$S_2O^{Mo-100S}$ (trigonal planar)~Ni $-S_2^{S-100S}$ (angular) » Ni–O^{S-100S} (linear). Therefore, Ni_{SA} metal centers were not preferentially occupying the V_S sites (Ni–O^{S-100S} coordination), but they were both occupying four-fold square planar sites above S atoms in the Mo-terminated surface (−41.9 kcal mol^{-1}, see Supporting Information S1: Figure S4A) and two-fold angular sites above S atoms in the S-terminated surface (−25.1 kcal mol^{-1}, see Supporting Information S1: Figure S4B).

2.3 | Catalytic Performance Evaluation Toward Co_2 Hydrogenation

The photocatalytic capacity of molybdenum MoO_xS_y for the gas-phase CO_2 reduction was tested under LED-UV excitation at 365 nm (Figure 5). The main reaction by-products were CO and, to a minor extent, CH_4. The productivity of CO roughly doubled (from 0.13 to 0.25 mmol/(g_{cat} h)) when Ni was photodeposited in MoO_xS_y. In contrast, CH_4 productivity decreased from 0.03 mmol/(g_{cat} h) down to 0.01 mmol/(g_{cat} h) after the Ni photodeposition (Figure 5B). A minimal C_2H_6 productivity (lower than 1 μmol/(g_{cat} h)) could be detected over both MoO_xS_y and Ni–MoO_xS_y (Figure 5A,B). The final conversion after 15 h in batch mode increased from 3.2% to 8.7% after Ni photodeposition and, on average, the kinetics of CO_2 conversion was three times faster (Figure 5C).

Operating under continuous conditions gave rise to a remarkable increase in the productivity of the Ni–MoO_xS_y catalyst with a noticeable increase in selectivity toward CO (Figure 5D) under excitation with different LEDs ranging from the visible to the near-infrared (NIR) window. MoO_xS_y (Figure 5D), on the other hand, exhibited similar productivity values of CO and CH_4 somewhat higher but similar to those obtained in the batch tests. Initially, CO_2 hydrogenation was conducted under illumination at 365 nm, showing CO and CH_4 productivities close to 0.2 and 0.02 mmol/(g_{cat} h) for MoO_xS_y. Switching the irradiation to RGB white light under the same gas flow and temperature conditions induced a sharp reduction of CO and CH_4 productivities by a 50% factor in comparison with the 365 nm or even 940 nm illumination. However, a second period of UV-A irradiation increased the production of CO and CH_4 up to 0.65 and 0.2 mmol/(g_{cat} h), which remained roughly constant after 20 h of continuous reaction.

The Ni–MoO_xS_y catalyst exhibited a very significant enhancement in CO_2 conversion and selectivity to CO in comparison with the Ni-free catalyst, reaching much higher productivity values at each condition (Figure 5D). Thus, CO and CH_4 productivities reached up to 5.1 and 0.2 mmol/(g_{cat} h) in the initial UV-A illumination stage (Figure 5E). Then, illumination under the RGB white light and the NIR LEDs at 250°C led to CO productivity values of 3.1 mmol/(g_{cat} h) and increased up to 2.8 mmol/(g_{cat} h), respectively (Figure 5E). The final irradiation with UV-A light at 365 nm increased the CO productivity strongly, reaching over 5 mmol/(g_{cat} h) for over half an hour, stabilizing around 3.3 mmol/(g_{cat} h) until the end of the 20-h photocatalytic test. In comparison, thermal experiments at 250°C avoiding light exposure under continuous flow conditions showed maximum CO and CH_4 productivities over MoO_xS_y around 0.25 and 0.13 mmol/(g_{cat} h). Following the introduction of Ni, a large increase in productivity was observed also for thermal experiments, reaching values around 1.4 mmol/(g_{cat} h) for CO and 0.1 mmol/(g_{cat} h) for CH_4, respectively (see Supporting Information S1: Figure S5), and the CO productivity was less than that of the same catalyst under UV illumination. These results suggest that a photonic contribution to the CO_2 reduction could be attributed to Ni–MoO_xS_y not only under UV irradiation, where the difference is highest, but also under visible and infrared regimes (see Figure 5D).

These results are in good agreement with recent reports on the photocatalytic CO_2 hydrogenation over MoS_2-like materials. Though most of the experimental tests were in the aqueous phase, using CO_2-saturated solutions as reaction media (Table 1 and references therein), CO or CH_3OH was the main obtained products, depending on the reaction conditions, such as temperature.

2.3.1 | In-Situ DRIFTS Analysis of the Thermal Catalytic Process

Interestingly, both RWGS and Sabatier reactions would take place through the dissociation of surface-adsorbed CO_2 into CO that evolves either to formate or to carbide to yield CH_4 upon further hydrogenation [66]. To unravel the reaction mechanisms over the tested catalysts, the CO_2 adsorption and further reaction with H_2 in a 1:4 gas flow ratio was followed by in situ DRIFTS analysis at the reaction conditions. At first, CO_2 gas was adsorbed on the catalyst surface (Figure 6) as it was identified by the presence of the ν_3 stretching band around 2340 cm^{-1} and the stretching ν_1 around 600 cm^{-1}, as well as combination bands about 3600 cm^{-1} (see Supporting Information S1: Figures S6 and S7). In addition, a band of about 2077 cm^{-1} corresponding to surface-active adsorbed CO_2 molecules (marked as CO_2* in Figure 6) could be also identified [67], whose intensity increased as exposure time in CO_2 flow increased (Figure 6A). The adsorbed CO_2 was identified through the formation of C–O stretching bands around 1000 cm^{-1} (Figure 6B), corresponding to bridged carbonate

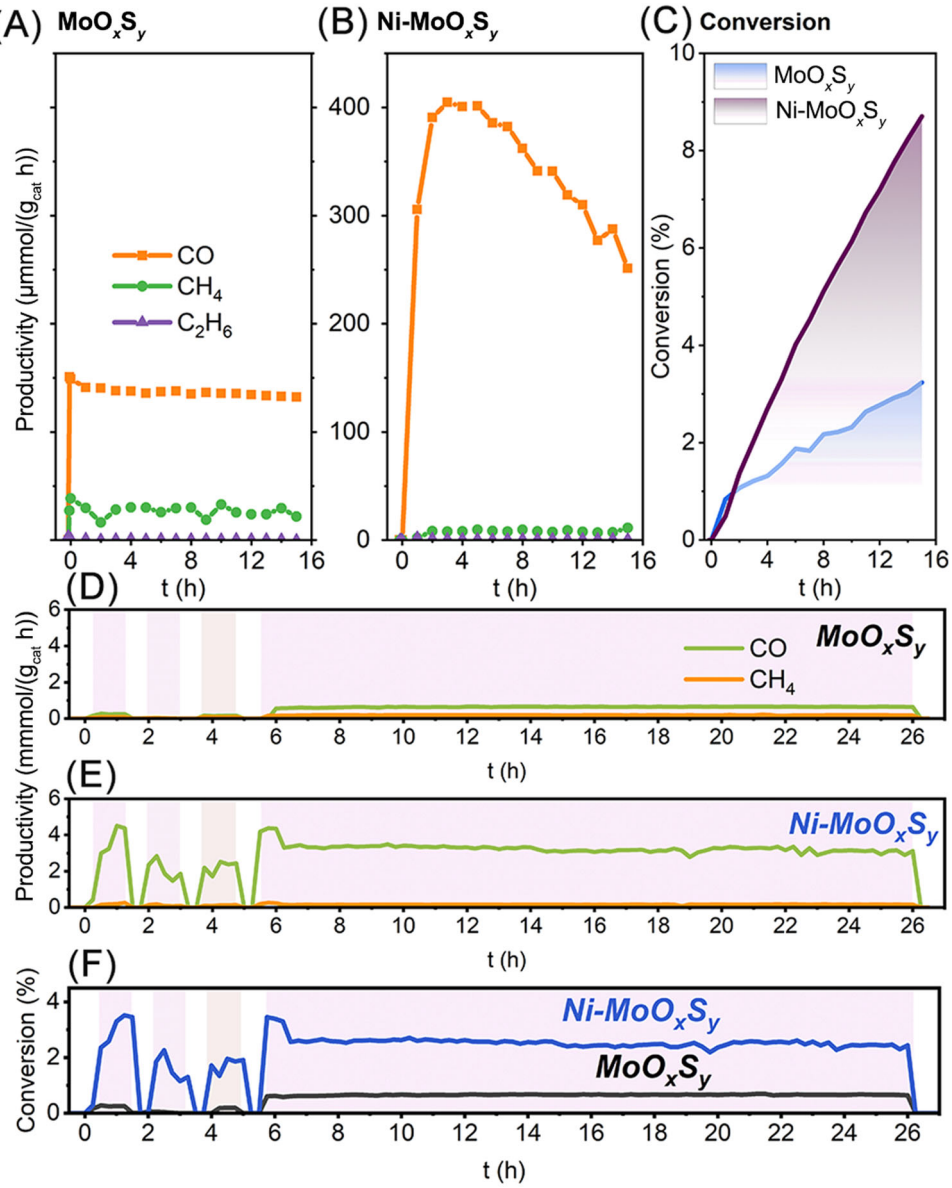

FIGURE 5 | Photocatalytic response of Ni-supported molybdenum oxysulfide catalysts under (A–C) batch and (D) continuous flow modes: productivity of CO and CH_4 versus time plots for (A) MoO_xS_y and (B) Ni–MoO_xS_y; (C) evolution of CO_2 conversion for both catalysts ($CO_2/H_2 = 1/4$, 15 mL/min in STP, $p = 1.7$ bar, under LED irradiation at 365 nm and 250°C); (D, E) sequential continuous CO_2 hydrogenation under UV (365 nm), visible (RGB), infrared (940 nm), and final UV (365 nm) irradiation ($CO_2/H_2 = 1/4$, 15 mL/min in STP, $p = 1.7$ bar) for both catalysts and (F) evolution of CO_2 conversion in the sequential conditions for hydrogenation.

(–CO_3) groups linked to Mo atoms through oxide anions (Figure 6B). These suggest that oxide species on oxysulfides favored the adsorption of CO_2, increasing the concentration of surface oxide groups (Figure 6A). Even more intense bands at the same wavelengths were observed for Ni–MoO_xS_y, suggesting a larger degree of CO_2 adsorption over the catalyst surface (Figure 6B).

Under the CO_2/H_2 stream at 250°C (Figure 6C,D), bands attributed to surface-linked carbonate and formate species were identified with clear differences for the Ni-containing material. For MoO_xS_y, bands attributed to the bending mode (δ) of gas phase water around 1645 cm^{-1} (Figure 6C) showed up at the beginning of the reaction. These were progressively overlapped with the bending vibrations of polydentate carbonate (–CO_3), hydrogen carbonate (–CO_3H), and bridged formate species (–CO_2H), which were expected in the context of CO_2 reduction reactions over metal oxide and sulfide catalysts [33, 68]. The band at 1578 cm^{-1} was assigned to the formation of surface monodentate –CO_2H species, together with the most intense signal at 1243 cm^{-1} corresponding to monodentate –CO_3H species. The shoulder at 1140 cm^{-1} was attributed to bridged –CO_3H species [42]. The intensity of CO_2* bands decreased as the reaction proceeded over the catalyst, which suggested the reduction of adsorbed species toward CO and H_2O. This could explain the initial reaction burst observed in the photocatalysis experiments (Figure 5A,B). The formation of a large amount of surface water upon the reaction of CO_2 and H_2 was observed over

TABLE 1 | Summary of photocatalytic or catalytic CO_2 reduction over different MoS_2-based 2D materials.

Catalyst	Reaction conditions	Light source	Irradiance (W/m^2)	Productivity ($mmol/(g_{cat}\,h)$)
Ag NP (20% wt.) on exfoliated MoS_2 [58]	i-C_3H_7OH and CO_2, 20°C	250 W Hg lamp		(Batch reactor) 0.365 (CH_3OH)
MoS_2 nanosheets over *h*-BN nanoplatelets [59]	50 mL of 2:1 mixture of H_2O and $(C_2H_5)_3NH$ bubbled with CO_2 until saturation, room temperature and pressure	20 W white LED	1760.4 lx	(Batch reactor) 6 (CH_3OH)
In_2S_3/MoO_3@MoS_2 heterojunctions [60]	Xe lamp was 200 mW cm^{-2} ($\lambda > 420$ nm), 10 mL H_2O, and 5 mL CO_2, 150°C			(Batch reactor) 0.23 (CO) 0.13 (CH_4)
Sulfur vacancy-rich few layers MoS_2 [33]	0.16 mL/min H_2/CO_2 3:1, 50 bar, 180°C	Thermal catalysis	Thermal catalysis	2010 (CH_3OH)
MoS_2 in mesoporous N-doped C [61]	450–650°C, 1 atm, 60 mL/min, H_2:CO_2:N_2 in the ratio of 4:1:0.56	Thermal catalysis	Thermal catalysis	17–35 (CO)
2D/1D MoS_2/TiO_2 heterojunctions [62]	CO_2 gas and H_2O vapor in situ produced by injection of 0.35 mL HCl aqueous solution in a 150 mL quartz reactor with 30.12 g of $NaHCO_3$	Sunlight irradiation 300 mW cm^{-2} (AM 1.5G Xe lamp) visible light (300 mW cm^{-2}, 400–1200 nm)		(Batch reactor) 0.035 (CO solar irradiation) 0.08 (CH_4 visible light)
Edge-sulfur vacancies of MoS_2 [63]	20 mg catalyst in 0.5-M $KHCO_3$ with 0.5 MPa to 4.5 MPa of $CO_2/H_2 = 1/3$ gas at 200°C for 10 h	Thermal catalysis	Thermal catalysis	0.8–14.6 (HCO^-)
MoS_2 on mesoporous g-C_3N_4 [64]	5 mL water saturated with CO_2, simulated solar light			(Batch reactor) 2 (CO)
Co-doped MoS_2-COF nanospheres [65]	4 mL of CH_3CN added into a 50-ml glass reactor, $p(CO_2) = 1$ atm	Visible light		(Batch reactor) 0.2 (CO)

Ni–MoO_xS_y. The increase of the stretching bands of adsorbed water molecules at about 3500 cm^{-1} (see Supporting Information S1: Figure S7) and the bending δ-modes of OH groups at 1623 cm^{-1} suggested that Ni-containing material favored the reduction reaction to a larger extent than MoO_xS_y. The band at 1348 cm^{-1} pointed out the rapid formation of polydentate hydrogen carbonate (–CO_3H) species, as well as the peak at 1245 cm^{-1} due to monodentate –CO_3H groups. This noticeably large presence of hydrogen carbonate groups over Ni-containing catalysts could clarify the enhanced CO productivity detected for these catalysts since those favored the RWGS reaction over Sabatier's [69]. The intensity of bands in the 900–960 cm^{-1} region increased with time reaction with CO_2 and H_2 for both MoO_xS_y and Ni–MoO_xS_y (Figure 6C,D). These had been typically attributed to the formation of oxysulfides where the Mo=O groups were formed by direct link through sulfide anions at the surface [33, 70], suggesting that those groups might play a role in the catalytic process. The increase in surface concentration of Mo^{4+} after photocatalytic tests (Figure 3D) would suggest that these Mo=O and Mo–O–Mo units detected in DRIFTS spectra were formed at the beginning of the reaction and evolved into MoS_2 and MoO_3 as the reaction time increased.

In summary, the adsorbed CO_2 molecules on Ni-free catalysts reacted with H_2 to render polydentate bicarbonates and formates that were further released as CO and H_2O molecules. On the other hand, Ni–MoO_xS_y was covered with a higher content of bicarbonates, mainly monodentate, which released a larger amount of H_2O and CO than the Ni-free catalysts. Surface formates were more evident in MoO_xS_y, suggesting a more effective Sabatier's reaction over those than in the case of Ni-doped substrates. Nevertheless, the production of CH_4 was small in both cases, suggesting that a hydrogenation cocatalyst would be necessary in these materials to shift the reaction equilibria towards hydrocarbons.

2.4 | Modeling of the Adsorption Configurations of H_2 and CO_2

The different adsorption steps on Ni-doped MoS_xO_y for CO_2 and H_2 were systematically studied depending on experimental conditions. The physisorbed H_2 configuration (Figure 7) was found when the Ni atom has high coordination environments (Mo edges), and the H_2 molecule is adsorbed on Ni with low

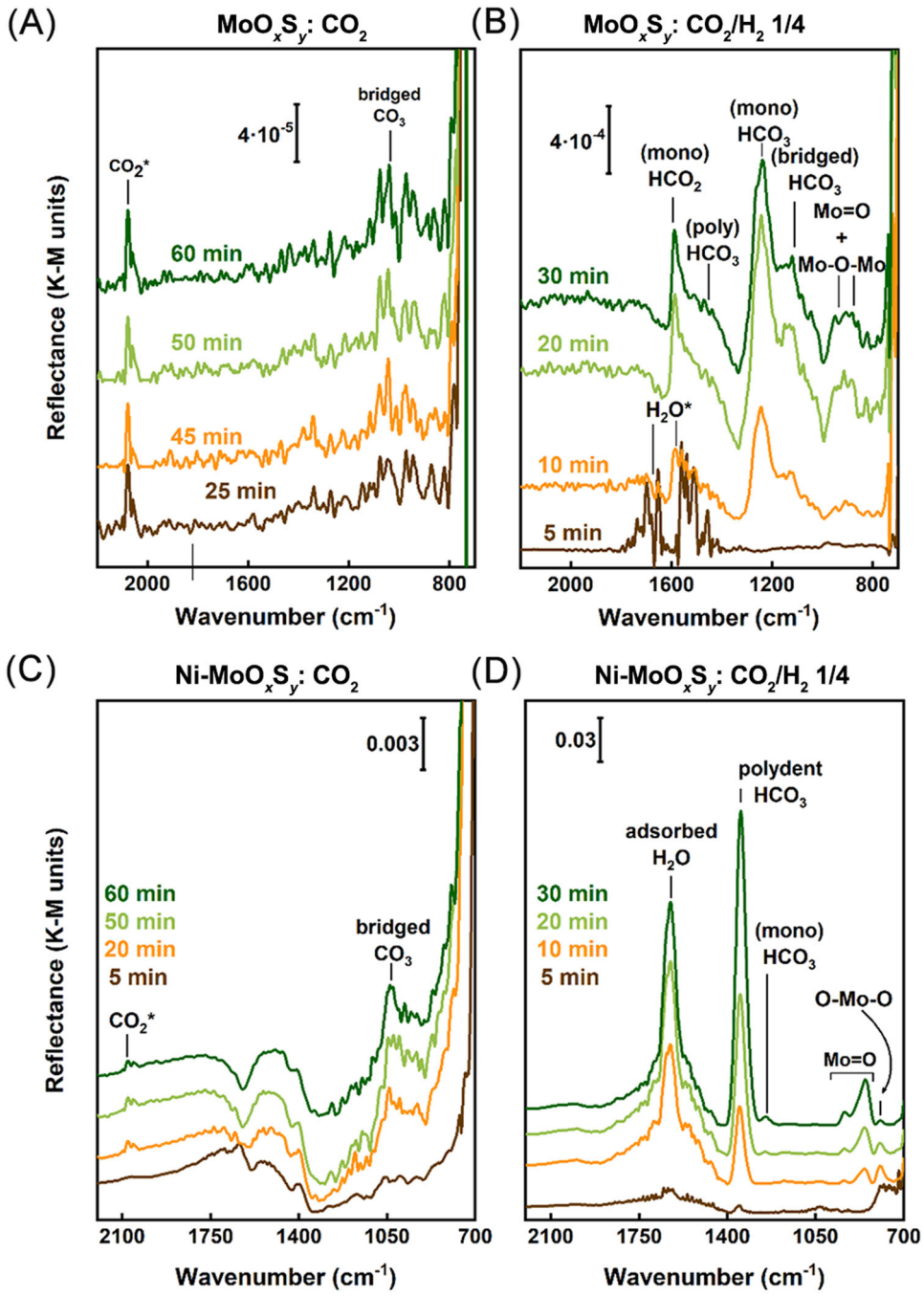

FIGURE 6 | In situ DRIFTS spectra of the CO_2 adsorption at 250°C (5 mL/min in STP and $p = 1$ bar) over (A) MoO_xS_y and (B) Ni–MoO_xS_y showing the time-based increase of CO_2* and bridged carbonate bands up to 60 min of exposure; in situ DRIFTS spectra under reaction conditions ($CO_2/H_2 = 1/4$, 15 mL/min in STP, $p = 1$ bar) showing the increase in HCO_2 and HCO_3 stretching bands, together with the formation of Mo–O species over (C) MoO_xS_y and (D) Ni–MoO_xS_y at the beginning of surface reaction. Notice the increase of H_2O δ bands (1623 cm^{-1}) on the Ni–MoO_xS_y (D) surface upon CO_2 reduction reaction.

coordination environments (S edge, adsorption free energy of -0.6 kcal mol^{-1}). CO_2 adsorption presented an even more accentuated coordinative preference, being the most stable also on the NiS_2 environment (adsorption free energy of 4.2 kcal mol^{-1}), with the ∠C–O–C angle bent to 149° and the C–O bond length elongated by 0.08 Å (1.26 vs. 1.18 Å in gas phase), similarly to those reported for Co/MoS_2 catalysts [71]. As a result, the greater structural stability of Ni_{SA} on Mo-terminated structures made them less reactive (since they are less exposed on the surface) than Ni_{SA} stabilized on S-terminated structures, and hence, only the NiS_2 anchorage on the S-100S defective edge model was taken into account as coordination environment in this study.

With a remarkable activity to bind and promote these molecules, H_2 dissociation pathways on Ni_{SA}/MoS_xO_y materials for subsequent catalytic conversion of CO_2 were systematically explored. Five possible configurations were identified for the generated H atoms, that is, H attached on Ni_{SA}, on a fully coordinated O or S atom, on the O atom neighboring the V_S, or

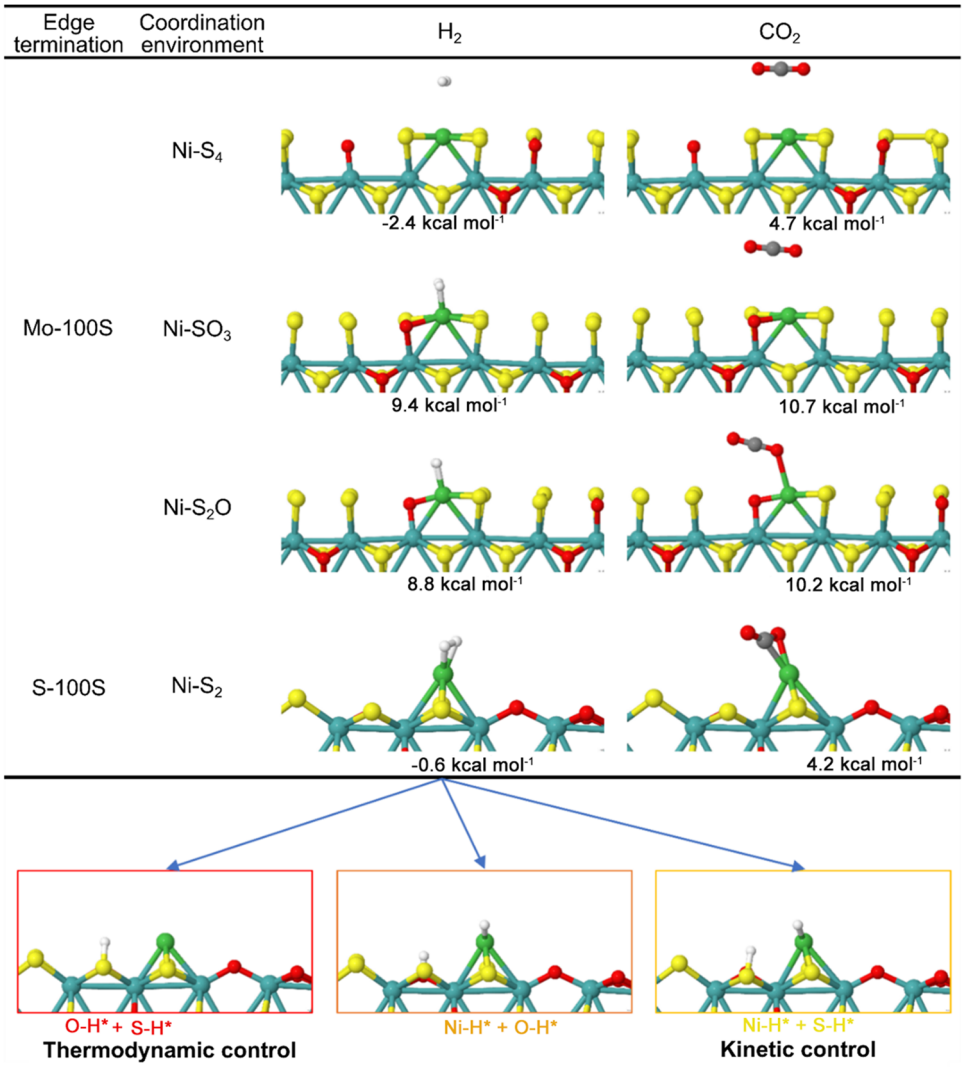

FIGURE 7 | (Top) Most stable adsorption configurations and corresponding adsorption free energies (G_{ads}) of H_2 and CO_2 on the different coordination environments of Ni-supported MoS_xO_y catalysts. The energy is defined as $G_{ads} = G_{X@Ni/MoS_xO_y^{\#}} - G_{Ni/MoS_xO_y^{\#}} - G_X$, where the $G_{X@Ni/MoS_xO_y^{\#}}$, $G_{Ni/MoS_xO_y^{\#}}$, and G_X represent the total free energy of the adsorbed molecule on the defective Ni_{SA} edge model, the clean defective Ni_{SA} edge model, and the isolated molecule, respectively. (Bottom) Dissociative adsorption of H_2 to 2H* on the NiS_2 coordination environment of the S-100S defective edge model. The symbol * Denotes surface-adsorbed species. Atomic color scheme: Mo (Verdigris); Ni (Apple); S (Daffodil); O (Candy Apple Red); C (Philippine Gray); H (White).

on the V_S itself (Supporting Information S1: Figure S8). Once adsorbed on the metal center, the H_2 molecule can dissociate by transferring H atoms to the nearby saturated O and S atoms (O–H* + S–H*). This scenario turned out to be the most thermodynamically favorable with a dissociative adsorption barrier of 28.2 kcal mol^{-1}. The H_2 dissociation process with H atoms captured by the Ni_{SA} and the nearby saturated O atom (Ni–H* + O–H*) was found energetically challenging (Figure 7). However, both scenarios were less favorable from a kinetic point of view than the scenario with H atoms captured by the Ni_{SA} and the nearby saturated S atom (Ni–H* + S–H* [72]), with a low energy barrier of 17.1 kcal mol^{-1}. The H atoms captured by the metal center and the O atom neighboring the V_S or the V_S itself (Ni–H* + O_{SA}–H* and Ni–H* + V_S–H*, see Supporting Information S1: Figure S8) barely produced plausible scenarios from a thermodynamic standpoint. Finally, the dissociation of H_2 resulting in two attached H atoms on the Ni_{SA} was unfavorable, since all tested geometry optimizations converged to undissociated H_2. These results suggested competing pathways leading to different hydrogen species for H_2 dissociation on the S-terminated MoS_xO_y surface. The O–H* + S–H* configuration was then the thermodynamic speciation and was favored under thermodynamic control while Ni–H* + S–H* was the kinetic speciation, favored under kinetic control.

2.4.1 | Mechanistic Studies of CO_2 Reduction Reaction

Commonly, two possible reduction pathways from chemisorbed CO_2 are considered: (i) the RWGS conversion and (ii) the formate pathway [73]. Since reaction conditions affected surface-adsorbed H atoms, both reduction pathways through two reaction controls were considered. At the reaction temperature (250°C), thermodynamic control was presumably predominant where the free energy profile (Figure 8) of the CO_2 reduction

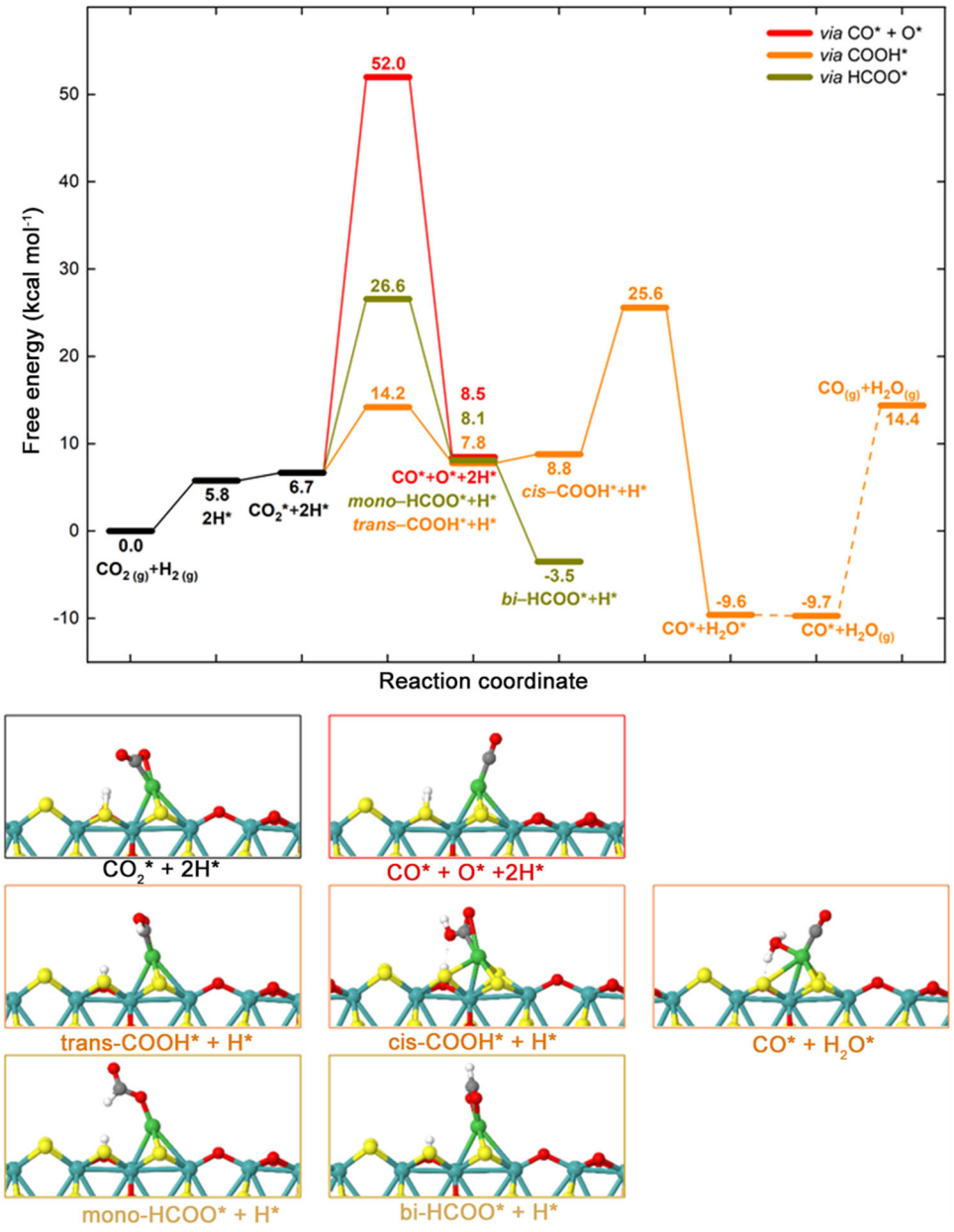

FIGURE 8 | Free energy profiles and optimized structures for the reduction reaction of CO_2 under thermodynamic control on the Ni_{SA}/MoS_xO_y catalyst model: to CO via direct dissociation (in red) and carboxyl (in orange) intermediate; and to HCOO species via formate (in the dark yellow) intermediates (black for the initial common steps). The energy is referenced with respect to the Ni-supported catalyst, $H_{2(g)}$, and $CO_{2(g)}$. Atomic color scheme: Mo (Verdigris); Ni (Apple); S (Daffodil); O (Candy Apple Red); C (Philippine Gray); H (White).

started from the H_2 dissociative adsorption on the surface (O–H* + S–H*). The CO_2 coordination on the Ni_{SA} was enhanced with respect to the non-hydrogenated edge, suggesting that higher H-coverage environments could activate adsorbates and benefit the hydrogenation reaction as reported for MoC_x [74]. The energetics showed that CO_2 would hardly be able to dissociate directly into CO* and O*, needing to overcome a high effective energy barrier of 52.0 kcal mol^{-1} (Figure 8, red pathway).

The dissociative reaction mechanism would preferentially take place on other Mo-based catalysts, such as on S vacancies in MoS_2 edges or supported Mo_2C clusters [33, 75]. However, it might be hydrogenated in the first stage to carboxyl species (COOH) as an intermediate in the RWGS reaction via the Langmuir–Hinshelwood (LH) mechanism. The associative formation of *trans*–COOH* (relative configuration with the new O–H bond on the opposite side of the C=O) was kinetically favorable with a reduced effective energy barrier of 14.2 kcal mol^{-1} (Figure 8, orange pathway). In these conditions, with H atoms of different nature, the H atom attacking the adsorbate was always the closest to hydrogenation, here the surface S–H*. Remarkably, it was not possible to simultaneously obtain CO* and OH* moieties on the metal center, either by hydrogenative dissociation of the adsorbed CO_2 or by successive dissociation of *trans*–COOH*, which contrasted with the foremost mechanism on basal plane-based Co/MoS_2 catalysts [71].

By means of a geometric isomerization to *cis*–COOH, the organic moiety was arranged aiming directionally towards the adsorbed O–H*. Its subsequent hydrogenative dissociation into CO* and H_2O* was clearly exergonic and the potential most energy-demanding step with an effective energy barrier of 25.6 kcal mol^{-1}. The H_2O molecule would further undergo thermoneutral desorption, while the CO desorption had an endergonic energy of 24.1 kcal mol^{-1}, in agreement with the abundance of adsorbed water experimentally observed from the reaction start by DRIFTS (Figure 6). It was confirmed that H_2O* was also substantially produced by the surface reaction step between H* species (from S–H* to O–H*, see Supporting Information S1: Figure S9). Furthermore, to delve deeper into the initial mechanisms of adsorbed CO_2 reduction, the formation of formate species (HCOO) was also considered as a possible competitive reaction pathway with the formation of CO on Ni_{SA}. An effective energy barrier of 26.6 kcal mol^{-1} (Figure 8, dark yellow pathway) was identified for the formation of the monodentate *mono*–HCOO* adsorbate through the LH mechanism, which was higher than that of *cis*–COOH formation. This could explain the low presence of dentate-like adsorbed species detected at short reaction times by DRIFTS (Figure 6D). Considering the spontaneous interconversion from *mono*–-HCOO* to bidentate *bi*–HCOO* adsorbates, the extensive dominance of polydentate versus monodentate species at long reaction times was assumed. Consequently, CO_2 molecules were first hydrogenated into carboxyl COOH which, after hydrogenation, dissociated into CO and H_2O over Ni–MoS_xO_y (Figure 8). Direct dissociation into CO* and O* was minor due to the higher energy barrier, and further hydrogenation to formate HCOO was only noticeable over long reaction times.

In contrast, kinetic control aimed to be less prominent. In this scenario, the Ni–H* + S–H* species were inevitably formed faster and predominate. From the H_2 dissociative adsorption, the CO_2 activation on Ni_{SA} turned out to be weaker than that in the thermodynamic control and at the unhydrogenated edge, clearly pointing to the metal center with low capability to simultaneously capture H atoms and coordinate the adsorbate (see Supporting Information S1: Figure S10). Results pointed out that CO_2 cannot spontaneously dissociate into either CO* and O*, needing to overcome a very high effective energy barrier of 79.0 kcal mol^{-1} (Figure 8, red pathway). Under this kinetic control scenario, the hydrogenation of adsorbed CO_2 by the LH mechanism would require a lower effective energy barrier for *mono*–HCOO* formate species via Ni–H* (21.3 kcal mol^{-1}, Figure 8, dark yellow pathway) than that of the carboxyl species *trans*–COOH* via S–H* (28.0 kcal mol^{-1}, Figure 8, orange pathway). Comparing the reaction energies and energy barriers, the carboxyl pathway could be barely considered a competitive mechanism for the formate pathway [71]. However, while the conversion of adsorbed *mono*–HCOO* to *bi*–HCOO* was energetically preferred, the possible reactivity of the COOH species certainly shifted toward non-dissociative hydrogenation into HCOOH* instead of dissociative into CO*. This mechanistic variant, although rather unfavorable compared to the HCOO path, was prompted by captured Ni–H* units as a hydrogen source, unlike adsorbed O–H* in the thermodynamic control scenario. This underlying mechanism revealed that the formation of HCOOH was unfavorable on Ni–MoS_xO_y as reported for similar catalysts [71]. On the other hand, the capture of H atoms by Ni_{SA} promoted the formation of formate species as a minority compared to carboxyl groups due to the thermodynamic control.

3 | Conclusions

The mixed oxide and sulfide structure of MoO_xS_y materials with MoS_2 layered structure and low crystallinity exhibited enhanced properties for the photocatalytic gas-phase reduction of CO_2 into valuable products, mainly CO and CH_4. This process occurred through the formation and further stabilization of anion vacancies on the material surface that favored gas adsorption. These vacancies, in turn, served as reaction sites for the CO_2 adsorption and reaction in an H_2-rich atmosphere. The reaction could proceed thermally but was enhanced under LED irradiation at mild temperatures. This CO_2 photocatalytic reduction was driven by the formation of surface carbonates that evolved into CO and CH_4 molecules.

The introduction of Ni had a remarkable effect on catalyst selectivity to CO. Nickel cations were deposited in the layered structure of MoO_xS_y materials by means of a photo-assisted precipitation route under LED-light irradiation at 365 nm. The incorporation of that Ni on the surface of materials allowed the formation of a mixed Ni–MoO_xS_y structure, enhancing the H_2 dissociation activity and CO_2 hydrogenation, leading to an enhanced CO_2 conversion into CO and CH_4 under both thermal and especially photocatalytic activity tests. CO_2 hydrogenation over both catalysts was driven by the formation of Mo-O-Mo units on the surface that enhanced the adsorption of gas reactants under the reaction conditions. The formation of these surface-active carbonate groups depended on the concentration of sulfur vacancies due to the rearrangement of surface structure in the presence of CO_2 and H_2 gas molecules under light irradiation at diverse wavelengths.

Finally, DFT simulations showed how Ni preferentially coordinates with the sulfur atoms exposed in the layer borders. Also, the sulfur vacancy formation follows an oxygen substitution, which favors the adsorption of the dissociated hydrogen atoms by the neighboring Ni. This further improves the hydrogenation of CO_2-adsorbed molecules in the Ni to CO. In summary, the introduction of Ni leads to efficient molybdenum oxysulfide catalysts, with a layered MoS_2-like structure, able to perform continuous gas-phase CO_2 hydrogenation under a range of wavelengths, from UV up to infrared with CO_2 conversion values comparable to the literature, but under milder and less propitious reaction conditions. This feature could be of interest for the development of photocatalytic devices with applications in CCU technologies.

4 | Experimental Section

4.1 | Synthesis of Low-Ordered MoO_xS_y and Photo-Assisted Ni Deposition

Nanostructured MoO_xS_y with low crystallinity was synthesized using a modification of the procedure described by Krishnamoorthy et al. [76] In brief, stoichiometric amounts of

ammonium molybdate tetrahydrate ($(NH_4)_6Mo_7O_{24}{\cdot}4H_2O$; Merck, Darmstadt, Germany) and thiourea ($(NH_2)_2C{=}S$; ACS reagent grade, ≥ 99.0%, Merck) were mixed in an aqueous solution and submitted to thermal treatment at 150°C in an autoclave for 20 h. The solid precipitate was dispersed in double-deionized water and centrifuged at 7500 rpm for 10 min to remove excess reagents, repeating this process three times. Finally, the obtained black solid was dried at 100°C for 10 h and subsequently ground in an agate mortar for 10 min.

Nanosized Ni clusters were deposited onto the MoO_xS_y surface using a photo-assisted precipitation method as described elsewhere [77]. To this end, 100 mg of solid MoO_xS_y and 55 mg of nickel chloride ($NiCl_2$, 98%, Sigma-Aldrich, St. Louis, Missouri) were dispersed in 8 mL of double-deionized water in a 20-mL Pyrex tube. This tube was sealed with a rubber septum. After 20 min of degasification under N_2 flow, 1 mL of methanol (CH_3OH) was added to the mixture and used as a "hole scavenger." All reagents and precursors were used without previous purification. The suspension was irradiated with UV light using two LED lamps (OSRAM LED Engin, Wilmington, Massachusetts) at 365 nm for 600 s under continuous magnetic stirring to induce the photocatalytic reduction of the Ni precursor. The obtained suspension was further centrifuged at 7500 rpm for 10 min, washed two to three times with double-deionized water, and dried at 100°C for 10 h. The final solid samples were stored in the dark for further use and characterization. These nanomaterials were prepared at the Nanoparticles Synthesis Unit 9 of the ICTS NANBIOSIS at the Institute of Nanoscience and Materials of Aragon and the University of Zaragoza.

4.2 | Characterization Techniques

The crystalline structure of the catalysts was identified by the XRD technique in a Bruker D8 Advance Diffractometer (Bruker Corporation, Billerica, Massachusetts) equipped with a (002)-oriented Ge crystal monochromator using the Cu $K\alpha_1$ line at 1.5405 Å using a Bragg–Brentano configuration. Transmission electron microscopy (TEM) was performed using an FEI TECNAI T20 microscope operated at 200 keV. Aberration-corrected scanning transmission electron microscopy (Cs-corrected STEM) images were acquired using a high-angle annular dark field detector in an FEI XFEG TITAN electron microscope (Hillsboro, Oregon) operated at 300 kV and equipped with a CETCOR Cs-probe corrector from CEOS GmbH (Heidelberg, Germany), allowing the formation of an electron probe of 0.08 nm. The geometric aberrations of the probe-forming system were controlled to allow a beam convergence of 24.7 mrad half-angle. Elemental analysis was carried out using an energy dispersive X-ray (EDX) detector for EDS experiments in scanning mode. EDS mapping was acquired with an Oxford Instrument (NanoAnalysis & Asylum Research, High Wycombe, UK) detector and analyzed with the built-in AZtec software. Samples were prepared by drop casting 5 μL of powder suspensions on a holey carbon TEM grid. XPS was obtained before and after reaction in a Kratos AXIS Ultra DLD surface spectrometer (Kratos Analytical Ltd., Durham, UK). Analysis of the samples by Raman spectroscopy was carried out under ambient conditions before and after the photocatalytic reaction test using a WITec Alpha 300. All the measurements were recorded with a 532-nm laser with 0.1 mW power.

4.3 | Photo-Assisted CO_2 Hydrogenation Tests

The CO_2 hydrogenation tests were conducted in a fixed-bed reactor (Supporting Information S1: Figure S11). Typically, 120 mg of powdered catalysts were packed in a prismatic quartz reactor leading to a 10 × 5 × 2 mm photocatalytic fixed bed. This was positioned between two LED units operating at different wavelengths, selected from 365 nm, white light (RGB), and 940 nm. Before irradiation, a gas mixture of CO_2 and H_2 with a 1:4 molar ratio was fed into the reactor for 30 min to ensure air removal from inside the reactor and the bed. The reactor could be operated in continuous (one pass) or in batch (recirculation) flow modes. For batch experiments, the reactor was closed and filled with the gas mixture until an absolute pressure of 1.7 bar was reached using a recirculating OEM pump (Verderflex M1500, Groeningen, Netherlands) driving a 15 mL/min (in STP) gas flow through the reactor circuit. The complete reaction system included a 500-mL expansion chamber to buffer pressure oscillations and provide enough total volume for gas sampling in prolonged experiments. To start the reaction up, LEDs were switched on, leading to a rapid temperature rise of the catalytic bed up to 250°C. The DC current of the LED was set at 0.9 A and voltage at 12 V during irradiation for all studied materials. The gas mixture from the reactor was periodically analyzed using an on-line Agilent 490 micro-GC analyzer (Agilent Technologies, Santa Clara, California) equipped with three columns: one 10-m molar sieve with a 5-m PPQ precolumn, a 10-m PBQ, and a 10 m CP-wax.

For the continuous catalytic and photocatalytic experiments, the 500-mL chamber was bypassed and a restriction valve was used to increase pressure up to 1.7 bar in the reactor, using a 15 mL/min (STP) gas flow. The photocatalytic activity was tested under the same LED irradiation wavelengths as in batch mode while keeping a constant temperature in the reactor by tuning the airflow refrigeration system. Thermal catalysis experiments were performed in a tubular quartz reactor placed within a tubular electric furnace. In all cases, downstream gases from the reactor were sampled every 15 min using the micro-GC system.

4.4 | Computational Details

Periodic DFT calculations were performed using the ab initio plane-wave pseudopotential approach as implemented in the Vienna Ab initio Simulation Package (VASP 5.4 [78, 79]). The Perdew–Burke–Ernzerhof [80] exchange-correlation functional within the spin-polarized generalized gradient approximation was chosen, and van der Waals interactions were taken into account through the Grimme's D3 method with zero-damping function [81]. The innermost electrons were replaced by a projector-augmented wave (PAW) approach [82, 83], while the valence monoelectronic states were expanded in a plane-wave basis set with a cut-off energy of 500 eV. Transition states were first located using the Climbing Image Nudged Elastic Band (CI-NEB) method [84, 85] and then appropriately optimized using the Quasi-Newton algorithm. They were shown to exhibit a single imaginary frequency by diagonalizing the numerical Hessian matrix, in which each atom was displaced with a step of 0.015 Å. Iterative relaxation of atomic positions

proceeded until the change in total energy between successive steps was less than 10^{-5} eV and the Hellmann–Feynman forces on any direction acting on the atoms were less than 0.02 eV $Å^{-1}$ in all structure optimization and 0.06 eV $Å^{-1}$ for transition state search. Further details on the DFT simulations of molybdenum oxysulfide monolayers and reaction mechanisms for CO_2 hydrogenation can be found in the Supporting Information.

4.5 | In-Situ Spectroscopic Techniques (EPR and DRIFTS)

Catalysts were investigated by in situ EPR spectroscopy on a Bruker EMX (Bruker, Ettlingen, Germany) instrument fitted with an ST4102 cavity and a variable temperature unit and quartz insert. Four different measurements were carried out: first, survey EPR spectra were obtained under liquid nitrogen cooling to identify the main signals for every tested material. EPR spectra of crystalline MoS_2 (Sigma-Aldrich) were acquired as a reference. Typically, a sample mass of 25 mg was immobilized with quartz wool in a 4-mm inner diameter quartz tube and placed in the cavity. The EPR spectra (9.45 GHz, 20 mW, 5G modulation amplitude at 100 kHz) were continuously acquired under gas flow upon the sample analysis. Before analysis, samples were degassed with a 100-mL/min (in STP) He stream and heated at 10°C/min up to 100°C for 1 h. Afterward, the EPR cavity was naturally cooled down to room temperature. Details on the in situ experiments can be found in the Supporting Information.

The DRIFTS analysis of catalysts was performed using a Harrick Praying-Mantis accessory (Harrick, Inc., Pleasantville, New York) coupled to a Bruker (Bruker Co., Billerica, Massachusetts) Vertex70 spectrometer. Before the analysis, powdered samples were submitted to thermal treatment for 12 h at 150°C to eliminate any ambient humidity. Dried samples were placed in a Harrick HVC-DRP high-temperature reaction chamber (equipped with 4-mm thick ZnSe infrared windows) and exposed to further thermal treatment for 3 h at 150°C under vacuum to eliminate the adsorbed ambient CO_2. The in situ reaction tests over the catalysts were performed using a combined CO_2:H_2 1:4 gas flow at 15 mL/min (in STP) at different temperatures (see Supporting Information S1: Figure S12 for further details).

Acknowledgments

Financial supports from the Spanish Ministry of Science and Universities through CEX2023-001286-S, PID2020-114926RB-I00, and CTQ2016-77144-R research projects are gratefully acknowledged. Researchers also thank collaboration through InterPHOT thematic network and "Conexion Fotocatalisis" CSIC hub. A. Sanz thanks the financial support for the MICINN Scholarship. We thank Dr. S. Irusta for her assistance in preliminary XPS measurements. The synthesis of materials has been performed by the Platform of Production of Biomaterials and Nanoparticles of the NANBIOSIS ICTS, more specifically by the Nanoparticle Synthesis Unit of the CIBER in Bioengineering, Biomaterials & Nanomedicine (CIBER-BBN). The TEM images were taken at the Laboratorio de Microscopias Avanzadas, Instituto de Nanociencia y Materiales de Aragón, Universidad de Zaragoza, Spain. The authors would like to acknowledge the use of Servicio General de Apoyo a la Investigación-SAI, Universidad de Zaragoza. J.N.-R. and I.C.G. thankfully acknowledge the computing resources through the "Calcul en Midi-Pyrénées" initiative CALMIP (projects p0812 and p1214), and CINES, IDRIS, and TGCC within the allocation 2022-A0120906649 carried out by GENCI.

Conflicts of Interest

The authors declare no conflicts of interest.

References

1. "Outcomes of the Glasgow Climate Change Conference—Advance Unedited Versions (AUVs) and List of Submissions From the Sessions in Glasgow." United Nations Climate Change (2021), https://unfccc.int/process-and-meetings/conferences/glasgow-climate-change-conference-october-november-2021/outcomes-of-the-glasgow-climate-change-conference.

2. N. Mac Dowell, P. S. Fennell, N. Shah, and G. C. Maitland, "The Role of CO_2 Capture and Utilization in Mitigating Climate Change," *Nature Climate Change* 7, no. 4 (2017): 243–249.

3. M. N. Anwar, A. Fayyaz, N. F. Sohail, et al., "CO_2 Utilization: Turning Greenhouse Gas Into Fuels and Valuable Products," *Journal of Environmental Management* 260 (2020): 110059.

4. A. Francis, S. S. Priya., S. H. Kumar, K. Sudhakar, and M. Tahir, "A Review on Recent Developments in Solar Photoreactors for Carbon Dioxide Conversion to Fuels," *Journal of CO2 Utilization* 47 (2021): 101515.

5. X. Gao and W. Yang, "Reaction: Key Issues of Solar-Driven CO_2 Conversion to Fuel," *Chem* 6, no. 5 (2020): 1041–1042.

6. A. Mustafa, B. G. Lougou, Y. Shuai, Z. Wang, and H. Tan, "Current Technology Development for CO_2 Utilization Into Solar Fuels and Chemicals: A Review," *Journal of Energy Chemistry* 49 (2020): 96–123.

7. T. Auger, J. Trüby, P. Balcombe, and I. Staffell, "The Future of Coal Investment, Trade, and Stranded Assets," *Joule* 5, no. 6 (2021): 1462–1484.

8. J. Mertens, C. Breyer, K. Arning, et al., "Carbon Capture and Utilization: More Than Hiding CO_2 for Some Time," *Joule* 7, no. 3 (2023): 442–449.

9. M. Aresta, A. Dibenedetto, and A. Angelini, "The Changing Paradigm in CO_2 Utilization," *Journal of CO2 Utilization* 3–4 (2013): 65–73.

10. M. Tahir and N. S. Amin, "Recycling of Carbon Dioxide to Renewable Fuels by Photocatalysis: Prospects and Challenges," *Renewable and Sustainable Energy Reviews* 25 (2013): 560–579.

11. J. L. White, M. F. Baruch, J. E. Pander, et al., "Light-Driven Heterogeneous Reduction of Carbon Dioxide: Photocatalysts and Photoelectrodes," *Chemical Reviews* 115, no. 23 (2015): 12888–12935.

12. J. Schneider, M. Matsuoka, M. Takeuchi, et al., "Understanding TiO_2 Photocatalysis: Mechanisms and Materials," *Chemical Reviews* 114, no. 19 (2014): 9919–9986.

13. E. Grabowska, M. Marchelek, M. Paszkiewicz-Gawron, and A. Zaleska-Medynska, "Metal Oxide Photocatalysts," in *Metal Oxide-Based Photocatalysis*, ed. A. Zaleska-Medynska (Amsterdam: Elsevier, 2018), 51–209.

14. R. Verma, R. Belgamwar, P. Chatterjee, R. Bericat-Vadell, J. Sa, and V. Polshettiwar, "Nickel-Laden Dendritic Plasmonic Colloidosomes of Black Gold: Forced Plasmon Mediated Photocatalytic CO_2 Hydrogenation," *ACS Nano* 17, no. 5 (2023): 4526–4538.

15. C. Tébar-Soler, V. Martin-Diaconescu, L. Simonelli, et al., "Low-Oxidation-State Ru Sites Stabilized in Carbon-Doped RuO_2 With Low-Temperature CO_2 Activation to Yield Methane," *Nature Materials* 22, no. 6 (2023): 762–768.

16. R. Liu, Z. Chen, Y. Yao, et al., "Recent Advancements in g-C_3N_4-Based Photocatalysts for Photocatalytic CO_2 Reduction: A Mini Review," *RSC Advances* 10, no. 49 (2020): 29408–29418.

17. H. C. Hsu, I. Shown, H. Y. Wei, et al., "Graphene Oxide as a Promising Photocatalyst for CO_2 to Methanol Conversion," *Nanoscale.* 5, no. 1 (2013): 262–268.

18. X. Liu, C. Chen, H. Ye, et al., "One-Step Hydrothermal Growth of Carbon Nanofibers and Insitu Assembly of Ag Nanowire@Carbon Nanofiber@Ag Nanoparticles Ternary Composites for Efficient Photocatalytic Removal of Organic Pollutants," *Carbon.* 131 (2018): 213–222.

19. D. Li, M. Kassymova, X. Cai, S. Q. Zang, and H. L. Jiang, "Photocatalytic CO_2 Reduction Over Metal-Organic Framework-Based Materials," *Coordination Chemistry Reviews* 412 (2020): 213262.

20. K. Li, B. Peng, and T. Peng, "Recent Advances in Heterogeneous Photocatalytic CO_2 Conversion to Solar Fuels," *ACS Catalysis* 6, no. 11 (2016): 7485–7527.

21. Y. Dong, P. Duchesne, A. Mohan, et al., "Shining Light on CO_2: From Materials Discovery to Photocatalyst, Photoreactor and Process Engineering," *Chemical Society Reviews* 49, no. 16 (2020): 5648–5663.

22. Y. Chen, G. Jia, Y. Hu, et al., "Two-Dimensional Nanomaterials for Photocatalytic CO_2 Reduction to Solar Fuels," *Sustainable Energy & Fuels* 1, no. 9 (2017): 1875–1898.

23. J. Di, J. Xia, H. Li, and Z. Liu, "Freestanding Atomically-Thin Two-Dimensional Materials Beyond Graphene Meeting Photocatalysis: Opportunities and Challenges," *Nano Energy* 35 (2017): 79–91.

24. D. Deng, K. S. Novoselov, Q. Fu, N. Zheng, Z. Tian, and X. Bao, "Catalysis With Two-Dimensional Materials and Their Heterostructures," *Nature Nanotechnology* 11, no. 3 (2016): 218–230.

25. C. Lai, N. An, B. Li, et al., "Future Roadmap on Nonmetal-Based 2D Ultrathin Nanomaterials for Photocatalysis," *Chemical Engineering Journal* 406 (2021): 126780.

26. Y. Xiao, J. Ji, L. Zhu, et al., "Regeneration of Zero-Valent Iron Powder by the Cocatalytic Effect of WS_2 in the Environmental Applications," *Chemical Engineering Journal* 383 (2020): 123158.

27. Z. Wang and B. Mi, "Environmental Applications of 2D Molybdenum Disulfide (MoS_2) Nanosheets," *Environmental Science & Technology* 51, no. 15 (2017): 8229–8244.

28. J. Wang, S. Lin, N. Tian, T. Ma, Y. Zhang, and H. Huang, "Nanostructured Metal Sulfides: Classification, Modification Strategy, and Solar-Driven CO_2 Reduction Application," *Advanced Functional Materials* 31, no. 9 (2021): 2008008.

29. Y. Sun, S. Gao, F. Lei, and Y. Xie, "Atomically-Thin Two-Dimensional Sheets for Understanding Active Sites in Catalysis," *Chemical Society Reviews* 44, no. 3 (2015): 623–636.

30. Y. Liu, H. Wang, X. Yuan, et al., "Roles of Sulfur-Edge Sites, Metal-Edge Sites, Terrace Sites, and Defects in Metal Sulfides for Photocatalysis," *Chem Catalysis* 1, no. 1 (2021): 44–68.

31. J. H. Han, H. K. Kim, B. Baek, et al., "Activation of the Basal Plane in Two Dimensional Transition Metal Chalcogenide Nanostructures," *Journal of the American Chemical Society* 140, no. 42 (2018): 13663–13671.

32. G. Liu, C. Kolodziej, R. Jin, et al., "MoS_2-Stratified CdS-$Cu_{2-x}S$ Core-Shell Nanorods for Highly Efficient Photocatalytic Hydrogen Production," *ACS Nano* 14, no. 5 (2020): 5468–5479.

33. J. Hu, L. Yu, J. Deng, et al., "Sulfur Vacancy-Rich Mos_2 as a Catalyst for the Hydrogenation of CO_2 to Methanol," *Nature Catalysis* 4, no. 3 (2021): 242–250.

34. Y. Li and A. I. Frenkel, "Deciphering the Local Environment of Single-Atom Catalysts With X-Ray Absorption Spectroscopy," *Accounts of Chemical Research* 54, no. 11 (2021): 2660–2669.

35. C. M. Wolff, P. D. Frischmann, M. Schulze, et al., "All-In-One Visible-Light-Driven Water Splitting by Combining Nanoparticulate and Molecular Co-Catalysts on CdS Nanorods," *Nature Energy* 3, no. 10 (2018): 862–869.

36. V. Dřínek, R. Yatskiv, M. Klementová, et al., "Spectroscopic Properties of Nanostructured Molybdenum Oxysulfide Deposits Fabricated by MoO_3 Evaporation in H_2S," *Materials Letters* 275 (2020): 128075.

37. J. C. Dupin, D. Gonbeau, I. Martin-Litas, P. Vinatier, and A. Levasseur, "Amorphous Oxysulfide Thin Films MO_yS_z (M = W, Mo, Ti) Xps Characterization: Structural and Electronic Pecularities," *Applied Surface Science* 173, no. 1–2 (2001): 140–150.

38. J. Li, X. Xu, B. Huang, Z. Lou, and B. Li, "Light-Induced in Situ Formation of a Nonmetallic Plasmonic MoS_2/MoO_{3-x} Heterostructure With Efficient Charge Transfer for CO_2 Reduction and SERS Detection," *ACS Applied Materials & Interfaces* 13, no. 8 (2021): 10047–10053.

39. G. Zhang and X. Wang, "Oxysulfide Semiconductors for Photocatalytic Overall Water Splitting With Visible Light," *Angewandte Chemie International Edition* 58, no. 44 (2019): 15580–15582.

40. C. Lee, H. Yan, L. E. Brus, T. F. Heinz, J. Hone, and S. Ryu, "Anomalous Lattice Vibrations of Single- and Few-Layer MoS_2," *ACS Nano* 4, no. 5 (2010): 2695–2700.

41. H. Li, Q. Zhang, C. C. R. Yap, et al., "From Bulk to Monolayer MoS_2: Evolution of Raman Scattering," *Advanced Functional Materials* 22, no. 7 (2012): 1385–1390.

42. H. Yu, Z. Zhuang, D. Li, et al., "Photo-Induced Synthesis of Molybdenum Oxide Quantum Dots for Surface-Enhanced Raman Scattering and Photothermal Therapy," *Journal of Materials Chemistry B* 8, no. 5 (2020): 1040–1048.

43. L. Cai, J. He, Q. Liu, et al., "Vacancy-Induced Ferromagnetism of MoS_2 Nanosheets," *Journal of the American Chemical Society* 137, no. 7 (2015): 2622–2627.

44. B. Deroide, Y. Bensimon, P. Belougne, and J. V. Zanchetta, "Lineshapes of ESR Signals and the Nature of Paramagnetic Species in Amorphous Molybdenum Sulfides," *Journal of Physics and Chemistry of Solids* 52, no. 7 (1991): 853–857.

45. Y. Chen, G. Zhang, Q. Ji, H. Liu, and J. Qu, "Triggering of Low-Valence Molybdenum in Multiphasic MoS_2 for Effective Reactive Oxygen Species Output in Catalytic Fenton-Like Reactions," *ACS Applied Materials & Interfaces* 11, no. 30 (2019): 26781–26788.

46. H. W. Wang, P. Skeldon, and G. E. Thompson, "XPS Studies of MoS_2 Formation From Ammonium Tetrathiomolybdate Solutions," *Surface and Coatings Technology* 91, no. 3 (1997): 200–207.

47. C. K. Chua, A. H. Loo, and M. Pumera, "Top-Down and Bottom-Up Approaches in Engineering 1 T Phase Molybdenum Disulfide (MoS_2): Towards Highly Catalytically Active Materials," *Chemistry—A European Journal* 22, no. 40 (2016): 14336–14341.

48. L. Qiu and G. Xu, "Peak Overlaps and Corresponding Solutions in the X-Ray Photoelectron Spectroscopic Study of Hydrodesulfurization Catalysts," *Applied Surface Science* 256, no. 11 (2010): 3413–3417.

49. X. Y. Yu, Y. Feng, Y. Jeon, B. Guan, X. W. Lou, and U. Paik, "Formation of Ni-Co-MoS_2 Nanoboxes With Enhanced Electrocatalytic Activity for Hydrogen Evolution," *Advanced Materials* 28, no. 40 (2016): 9006–9011.

50. T. K. T. Ninh, L. Massin, D. Laurenti, and M. Vrinat, "A New Approach in the Evaluation of the Support Effect for NiMo Hydrodesulfurization Catalysts," *Applied Catalysis A: General* 407, no. 1–2 (2011): 29–39.

51. H. B. Yang, S. F. Hung, S. Liu, et al., "Atomically Dispersed Ni(I) as the Active Site for Electrochemical CO_2 Reduction," *Nature Energy* 3, no. 2 (2018): 140–147.

52. C. Tsai, F. Abild-Pedersen, and J. K. Nørskov, "Tuning the MoS_2 Edge-Site Activity for Hydrogen Evolution via Support Interactions," *Nano Letters* 14, no. 3 (2014): 1381–1387.

53. T. F. Jaramillo, K. P. Jørgensen, J. Bonde, J. H. Nielsen, S. Horch, and I. Chorkendorff, "Identification of Active Edge Sites for Electrochemical

H_2 Evolution From MoS_2 Nanocatalysts," *Science.* 317, no. 5834 (2007): 100–102.

54. Q. Xu, Y. Liu, H. Jiang, Y. Hu, H. Liu, and C. Li, "Unsaturated Sulfur Edge Engineering of Strongly Coupled MoS_2 Nanosheet–Carbon Macroporous Hybrid Catalyst for Enhanced Hydrogen Generation," *Advanced Energy Materials* 9, no. 2 (2019): 1802553.

55. Z. Zheng, S. Cong, W. Gong, et al., "Semiconductor SERS Enhancement Enabled by Oxygen Incorporation," *Nature Communications* 8, no. 1 (2017): 1993.

56. P. Zheng, T. Li, K. Chi, et al., "DFT Insights Into the Formation of Sulfur Vacancies Over Corner/Edge Site of Co/Ni-Promoted MoS_2 and WS_2 Under the Hydrodesulfurization Conditions," *Applied Catalysis B: Environmental* 257 (2019): 117937.

57. M. Sun, "On the Incorporation of Nickel and Cobalt Into MoS_2-Edge Structures," *Journal of Catalysis* 226, no. 1 (2004): 32–40.

58. Y. Zheng, X. Yin, Y. Jiang, et al., "Nano Ag-Decorated MoS_2 Nanosheets From 1T to 2H Phase Conversion for Photocatalytically Reducing CO_2 to Methanol," *Energy Technology* 7, no. 11 (2019): 1900582.

59. S. Kumari, R. Gusain, A. Kumar, N. Manwar, S. L. Jain, and O. P. Khatri, "Direct Growth of Nanostructural MoS_2 Over the h-BN Nanoplatelets: An Efficient Heterostructure for Visible Light Photoreduction of CO_2 to Methanol," *Journal of CO2 Utilization* 42 (2020): 101345.

60. F. Wang, D. Liu, J. Wen, and X. Zheng, "In-Situ Sulfurized In_2S_3/MoO_3@MoS_2 Heterojunction for Visible Light Induced CO_2 Photoreduction," *Journal of Environmental Chemical Engineering* 9, no. 5 (2021): 106042.

61. S. Sameer, G. Singh, J. Gahtori, et al., "Molybdenum Sulfide Embedded Mesoporous N-Doped Carbon as a Noble Metal-Free Highly Selective Catalyst for Conversion of CO_2 to CO," *Journal of Environmental Chemical Engineering* 10, no. 6 (2022): 108988.

62. A. Hezam, K. Alkanad, M. A. Bajiri, et al., "2D/1D MoS_2/TiO_2 Heterostructure Photocatalyst With a Switchable CO_2 Reduction Product," *Small Methods* 7, no. 1 (2023): 1–15.

63. Z. Wang, Y. Kang, J. Hu, et al., "Boosting CO_2 Hydrogenation to Formate Over Edge-Sulfur Vacancies of Molybdenum Disulfide," *Angewandte Chemie International Edition* 62, no. 45 (2023): e202307086.

64. V. Nair Gopalakrishnan, J. Becerra, S. Mohan, J. M. E. Ahad, F. Béland, and T. O. Do, "Cobalt-Doped MoS_2-Integrated Hollow Structured Covalent Organic Framework Nanospheres for the Effective Photoreduction of CO_2 Under Visible Light," *Energy & Fuels* 37, no. 3 (2023): 2329–2339.

65. N. Kumar, R. P. Mishra, B. Dash, S. Bastia, and Y. S. Chaudhary, "The Synergistic Chemical Coupling of Nanostructured MoS_2 With Nitrogen-Deficient 2-D Triazine-Based Polymeric m-C_3N_x for Efficient and Selective CO_2 Photocatalytic Conversion to Co," *Journal of Materials Chemistry A* 11, no. 38 (2023): 20839–20853.

66. C. Vogt, E. Groeneveld, G. Kamsma, et al., "Unravelling Structure Sensitivity in CO_2 Hydrogenation Over Nickel," *Nature Catalysis* 1, no. 2 (2018): 127–134.

67. S. M. Fehr and I. Krossing, "Spectroscopic Signatures of Pressurized Carbon Dioxide in Diffuse Reflectance Infrared Spectroscopy of Heterogeneous Catalysts," *ChemCatChem* 12, no. 9 (2020): 2622–2629.

68. F. Maugé, J. Lamotte, N. S. Nesterenko, O. Manoilova, and A. A. Tsyganenko, "FT-IR Study of Surface Properties of Unsupported MoS_2," *Catalysis Today* 70, no. 1–3 (2001): 271–284.

69. Y. Xie, X. Li, Y. Wang, et al., "Reaction Mechanisms for Reduction of CO_2 to CO on Monolayer MoS_2," *Applied Surface Science* 499 (2020): 143964.

70. E. Schmidt, C. Sourisseau, G. Meunier, and A. Levasseur, "Amorphous Molybdenum Oxysulfide Thin Films and Their Physical Characterization," *Thin Solid Films* 260, no. 1 (1995): 21–25.

71. Z. Lu, Y. Cheng, S. Li, Z. Yang, and R. Wu, "CO_2 Thermoreduction to Methanol on the MoS_2 Supported Single Co Atom Catalyst: A DFT Study," *Applied Surface Science* 528 (2020): 147047.

72. M. Sun, A. Nelson, and J. Adjaye, "Ab Initio DFT Study of Hydrogen Dissociation on MoS_2, NiMoS, and CoMoS: Mechanism, Kinetics, and Vibrational Frequencies," *Journal of Catalysis* 233, no. 2 (2005): 411–421.

73. M. González-Castaño, B. Dorneanu, and H. Arellano-García, "The Reverse Water Gas Shift Reaction: A Process Systems Engineering Perspective," *Reaction Chemistry & Engineering* 6, no. 6 (2021): 954–976.

74. M. Figueras, R. A. Gutiérrez, F. Viñes, P. J. Ramírez, J. A. Rodriguez, and F. Illas, "Supported Molybdenum Carbide Nanoparticles as an Excellent Catalyst for CO_2 Hydrogenation," *ACS Catalysis* 11, no. 15 (2021): 9679–9687.

75. J. Zhang, K. Feng, Z. Li, B. Yang, B. Yan, and K. H. Luo, "Defect-Driven Efficient Selective CO_2 Hydrogenation With Mo-Based Clusters," *JACS Au* 3, no. 10 (2023): 2736–2748.

76. K. Krishnamoorthy, G. K. Veerasubramani, S. Radhakrishnan, and S. J. Kim, "Supercapacitive Properties of Hydrothermally Synthesized Sphere Like MoS_2 Nanostructures," *Materials Research Bulletin* 50 (2014): 499–502.

77. A. Sanz-Marco, J. L. Hueso, V. Sebastian, et al., "Led-Driven Controlled Deposition of Ni Onto TiO_2 for Visible-Light Expanded Conversion of Carbon Dioxide Into C1–C2 Alkanes," *Nanoscale Advances* 3, no. 13 (2021): 3788–3798.

78. G. Kresse and J. Furthmüller, "Efficiency of Ab-Initio Total Energy Calculations for Metals and Semiconductors Using a Plane-Wave Basis Set," *Computational Materials Science* 6, no. 1 (1996): 15–50.

79. G. Kresse and J. Furthmüller, "Efficient Iterative Schemes for Ab Initio Total-Energy Calculations Using a Plane-Wave Basis Set," *Physical Review B* 54, no. 16 (1996): 11169–11186.

80. J. P. Perdew, K. Burke, and M. Ernzerhof, "Generalized Gradient Approximation Made Simple," *Physical Review Letters* 77, no. 18 (1996): 3865–3868.

81. S. Grimme, J. Antony, S. Ehrlich, and H. Krieg, "A Consistent and Accurate Ab Initio Parametrization of Density Functional Dispersion Correction (DFT-D) for the 94 Elements H-Pu," *Journal of Chemical Physics* 132, no. 15 (2010): 154104.

82. P. E. Blöchl, "Projector Augmented-Wave Method," *Physical Review B* 50, no. 24 (1994): 17953–17979.

83. G. Kresse and D. Joubert, "From Ultrasoft Pseudopotentials to the Projector Augmented-Wave Method," *Physical Review B* 59, no. 3 (1999): 1758–1775.

84. G. Henkelman, B. P. Uberuaga, and H. Jónsson, "A Climbing Image Nudged Elastic Band Method for Finding Saddle Points and Minimum Energy Paths," *Journal of Chemical Physics* 113, no. 22 (2000): 9901–9904.

85. G. Henkelman and H. Jónsson, "Improved Tangent Estimate in the Nudged Elastic Band Method for Finding Minimum Energy Paths and Saddle Points," *Journal of Chemical Physics* 113, no. 22 (2000): 9978–9985.

Supporting Information

Additional supporting information can be found online in the Supporting Information section.